

**Nucleon-induced reactions at intermediate energies: New data at 96 MeV and theoretical status**

V. Blideanu,<sup>1,\*</sup> F. R. Lecolley,<sup>1</sup> J. F. Lecolley,<sup>1</sup> T. Lefort,<sup>1</sup> N. Marie,<sup>1</sup> A. Ataç,<sup>2</sup> G. Ban,<sup>1</sup> B. Bergenwall,<sup>2</sup> J. Blomgren,<sup>2</sup> S. Dangtip,<sup>2,3</sup> K. Elmgren,<sup>4</sup> Ph. Eudes,<sup>5</sup> Y. Foucher,<sup>6</sup> A. Guertin,<sup>5</sup> F. Haddad,<sup>5</sup> A. Hildebrand,<sup>2</sup> C. Johansson,<sup>2</sup> O. Jonsson,<sup>7</sup> M. Kerveno,<sup>8</sup> T. Kirchner,<sup>5</sup> J. Klug,<sup>2</sup> Ch. Le Brun,<sup>9</sup> C. Lebrun,<sup>5</sup> M. Louvel,<sup>1</sup> P. Nadel-Turonski,<sup>10</sup> L. Nilsson,<sup>2,7</sup> N. Olsson,<sup>2,4</sup> S. Pomp,<sup>2</sup> A. V. Prokofiev,<sup>7</sup> P.-U. Renberg,<sup>7</sup> G. Rivière,<sup>5</sup> I. Slypen,<sup>11</sup> L. Stuttgé,<sup>8</sup> U. Tippawan,<sup>2,3</sup> and M. Österlund<sup>2</sup>

<sup>1</sup>*LPC, ENSICAEN, Université de Caen, CNRS/IN2P3, Caen, France*

<sup>2</sup>*Department of Neutron Research, Uppsala University, Sweden*

<sup>3</sup>*Fast Neutron Research Facility, Chiang Mai University, Thailand*

<sup>4</sup>*Swedish Defence Research Agency, Stockholm, Sweden*

<sup>5</sup>*SUBATECH, Université de Nantes, CNRS/IN2P3, France*

<sup>6</sup>*DSM/DAPNIA/SPhN, CEA Saclay, Gif-sur-Yvette, France*

<sup>7</sup>*The Svedberg Laboratory, Uppsala University, Sweden*

<sup>8</sup>*IReS, Strasbourg, France*

<sup>9</sup>*Laboratoire de Physique Subatomique et de Cosmologie, Grenoble, France*

<sup>10</sup>*Department of Radiation Sciences, Uppsala University, Sweden*

<sup>11</sup>*Institut de Physique Nucléaire, Université Catholique de Louvain, Louvain-la-Neuve, Belgium*

(Received 31 March 2004; published 15 July 2004)

Double-differential cross sections for light charged particle production (up to  $A=4$ ) were measured in 96 MeV neutron-induced reactions, at the TSL Laboratory Cyclotron in Uppsala (Sweden). Measurements for three targets, Fe, Pb, and U, were performed using two independent devices, SCANDAL and MEDLEY. The data were recorded with low-energy thresholds and for a wide angular range ( $20^\circ$ – $160^\circ$ ). The normalization procedure used to extract the cross sections is based on the  $np$  elastic scattering reaction that we measured and for which we present experimental results. A good control of the systematic uncertainties affecting the results is achieved. Calculations using the exciton model are reported. Two different theoretical approaches proposed to improve its predictive power regarding the complex particle emission are tested. The capabilities of each approach is illustrated by comparison with the 96 MeV data that we measured, and with other experimental results available in the literature.

DOI: 10.1103/PhysRevC.70.014607

PACS number(s): 25.40.-h, 24.10.-i, 28.20.-v

**I. INTRODUCTION**

The deep understanding of nucleon-induced reactions is a crucial step for the further development of nuclear reactions theory in general. In addition, complete information in this field is strongly needed for a large amount of applications, such as the incineration of nuclear waste with accelerator-driven systems (ADS), cancer therapy, or the control of radiation effects induced by terrestrial cosmic rays in microelectronics. For this reason, the problem of nucleon-induced reactions has gained renewed interest in the last few years. This interest has been expressed in part by extensive experimental campaigns, such as those carried out by several laboratories in Europe in the framework of the HINDAS program [1].

Particularly, nucleon-induced reactions in the 20–200 MeV energy range have for a long time been the subject of intensive theoretical studies. For this range, the first major step for the improvement of nuclear reaction models consisted of the introduction of the so-called “pre equilibrium process.” This process has been proposed in order to explain the smooth dependence of the particle emission

probability versus angle and energy, which has been observed experimentally. This preequilibrium process is supposed to occur at an intermediate stage and to consist of multiple nucleon-nucleon interactions that take place inside the target nucleus. During that process, particle emission occurs after completion of the one-step interaction phase, i.e., the direct process phase, but a long time before the statistical equilibrium of the compound nucleus has been reached.

During the last 40 years, several approaches attempted to give a theoretical description of this preequilibrium process. Some of them have shown all along a good predictive power for a wide set of experimental energy distributions of nucleons emitted in nucleon-nucleus reactions. However, those models were unable to reproduce the experimental distributions of complex particles, for which they systematically underestimate the production rates. Among them, the exciton model of Griffin [2] is a very good example. Originally introduced in 1966, this model has been quickly adopted by the community because of its adaptability and simplicity. In an attempt to increase its capability in reproducing the complex particle rates, two main approaches have been developed. The first one, proposed in 1973 [3], introduces a cluster formation probability during the nucleon-nucleon interactions inside the nucleus. The second one formulated by Kalbach in 1977 [4] is a completely different approach that takes into

\*Electronic address: blideanu@lpccaen.in2p3.fr

account the possible contributions of direct pick-up and knock-out mechanisms.

Nowadays, the exciton model modified according to these theories is the only one available to calculate energy spectra of both nucleons and complex particles emitted in nucleon-induced reactions at intermediate energies. In the past, both approaches have been tested against data, and they both show satisfactory agreement with experimental distributions [4,5]. The comparisons were made using the data available at that moment and that concern a limited number of reaction configurations and incident energies, lower than 63 MeV. Despite this success, several questions are still open to discussion. An extended study of the influence of the entrance channel parameters is necessary, i.e., the dependence on the incident particle type and on the incident energy has to be investigated.

The measurements presented in this work are part of the HINDAS program and they concern double-differential distributions of light charged particles, up to  $A=4$ , emitted in 96 MeV neutron-induced reactions on three targets: iron, lead and uranium. Calculations for those reactions are performed with the basic exciton model implemented in the GNASH code [6], and with both independent approaches proposed respectively by Ribanský and Obložinský [3] and by Kalbach [4]. The robustness of those approaches are also tested for other reactions with incident protons at lower energies and with other targets for which experimental results are available in the literature. This study allows a global view of the predictive power of each model.

The experimental setup used for data taking is briefly presented in Sec. II. In Sec. III, details concerning the procedures used to obtain the energy spectra and the cross section normalization are given. The results are presented in Sec. IV. Section V is dedicated to the description of the theoretical calculations related to the particle emission in nucleon-induced reactions at intermediate energies, and the predictions of the models are compared to experimental data. The conclusions of this work are given in Sec. VI.

## II. EXPERIMENTAL PROCEDURE

The experiments were performed using the neutron beam available at the TSL Laboratory in Uppsala (Sweden), whose facility is presented in Fig. 1. Neutrons were produced by  ${}^7\text{Li}(p,n){}^7\text{Be}$  reactions using a 100 MeV proton beam impinging on a lithium target. The beam monitoring was provided by a Faraday cup where the proton beam was dumped and by a fission detector composed of thin-film breakdown counters [7] placed in the experimental hall. The stability of the beam was checked regularly during the data taking. The deviations found between the indications of both monitors did not exceed 2%.

Difficulties encountered when working with neutron beams are related to their characteristics. The neutrons of the beam are not strictly mono energetic. This is illustrated in Fig. 2 where a typical neutron spectrum is shown. It presents two components: one is a peak centered at an energy slightly lower than the incident proton beam energy ( $Q = -1.6$  MeV), diminished of the energy loss inside the pro-

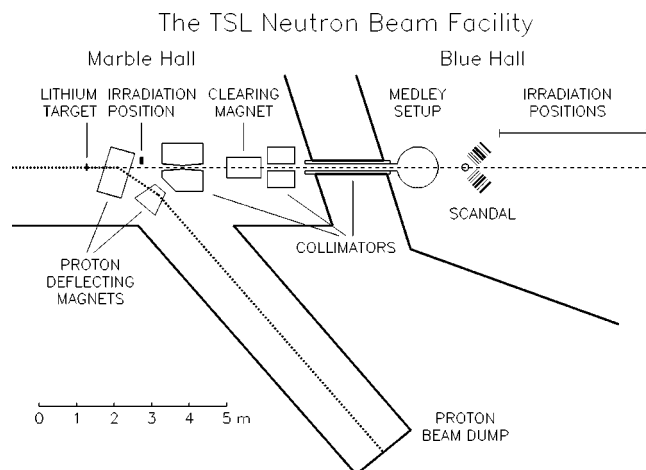


FIG. 1. TSL neutron beam facility and the location of the detection systems used in the experiment.

duction target, and the other is a low-energy tail that contains about 50% of the total number of produced neutrons, and which originates from highly excited states of  ${}^7\text{Be}$ . For the data analysis, events associated with low-energy neutrons must be rejected. The method employed for this rejection will be described in the forthcoming sections. After selection, the intensity of the resulting 96 MeV neutron beam is of the order of  $10^4$  n/cm<sup>2</sup> sec. The neutron beam is collimated to a solid angle of  $60\ \mu\text{sr}$  and the beam spot at about 10 m from the lithium target has a diameter of 8 cm (Fig. 2). These characteristics impose the use of an adequate detection setup in order to obtain a satisfactory counting rate, keeping, at the same time, the energy and angular resolutions within reasonable limits. Two independent detection systems, MEDLEY and SCANDAL, were used in our experiments. They were placed one after the other on the beam line as shown in Fig. 1.

### A. MEDLEY setup

The first setup downstream the beam was the MEDLEY detection array, described in detail in Ref. [8]. Composed of eight Si-Si-CsI telescopes, this system is used to detect light charged particles up to  $A=4$ , with a low-energy threshold and over an angular domain ranging from  $20^\circ$  to  $160^\circ$ , in steps of  $20^\circ$ . The telescopes were placed inside a vacuum reaction chamber of 100 cm diameter. The arrangement of the eight telescopes inside the chamber is given in Fig. 3. For the MEDLEY setup, the reaction target was placed at the center of the chamber and was tilted  $45^\circ$  with respect to the beam direction, in order to minimize the energy loss of the produced particles inside the target. Typically,  $50\ \mu\text{m}$  thick targets were used for all experiments. This allows small corrections for the energy loss of the emitted particles inside the target, but it also results in a low particle production rate. Due to the thin targets used and to the small solid angles of the telescopes, the statistics accumulated using the MEDLEY setup is relatively poor. The angular resolution was defined by the target active area and by the opening angle subtended by each telescope. It has been estimated

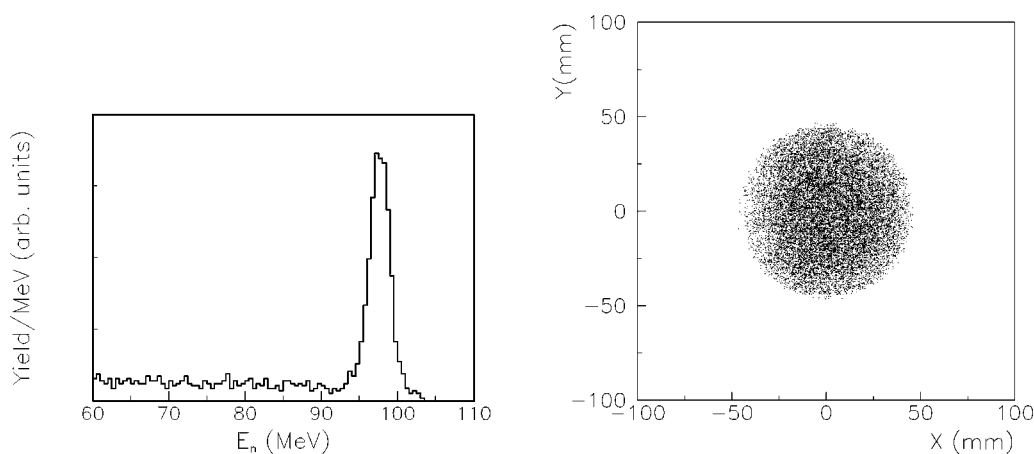


FIG. 2. Neutron energy spectra resulting from a 100 MeV proton beam on a 4 mm thick lithium target (left). Scatter plot showing the profile of the neutron beam at about 10 m from the lithium target (right).

using Monte Carlo simulations and typical values derived are of the order of  $5^\circ$ .

### B. SCANDAL setup

A detailed description of SCANDAL is given in Ref. [9]. It consists of two identical systems located on each side of the neutron beam and which covered a detection angular range of  $10^\circ$ – $140^\circ$  (Fig. 4). Since particles travel in air before entering the setup, only protons with energies larger than 30 MeV and a small number of deuterons could be detected. Each arm was composed of two 2 mm thick plastic scintillators used as triggers, two drift chambers used for the particle tracking, and an array of 12 CsI detectors enabling us to measure particle residual energies. The emission angle of each particle was determined from its trajectory through the drift chambers. With this method, the angular resolution was estimated to be of the order of  $1^\circ$ , which was a significant improvement compared to that obtained with the MEDLEY setup. An example of an angular distribution obtained with particles detected in one of the CsI detectors is shown, together with simulation results, in Fig. 5. The very good agreement observed is a necessary condition to demonstrate the validity of the tracking method used and the quality of the drift chambers. Using the trajectories, the coordinates

of the nuclear reactions on the target plane could be determined with a backtracking procedure. Since the SCANDAL targets were larger than the neutron beam, it was crucial to determine the active target area with good precision.

The SCANDAL setup had the particularity to operate with a multitarget system (MTGT) [10], which allows an increase of the counting rate without impairing the energy resolution. An expanded view of the system is given in Fig. 6. Up to seven targets, inserted between multiwire proportional counters (MWPC's), can be mounted simultaneously. The information given by MWPC's allows us to determine the target from which the particle has been emitted, and to apply corrections to the particle energy by taking into account the energy losses inside the subsequent targets. In addition, by mounting simultaneously targets of different elements, several nuclear reactions can be studied at the same time. During our experiments, we operated with seven targets: five targets were made of the same material and dedicated to the reactions under study (iron, lead, or uranium), another one was a pure carbon target, and the last one was a  $\text{CH}_2$  target. By these means, events associated with the reactions under study and events corresponding to the  $\text{H}(n,p)$  elastic scattering were recorded at the same time. As will be explained in

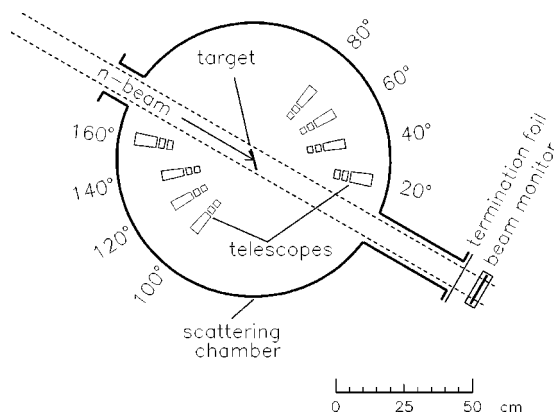


FIG. 3. MEDLEY detection array.

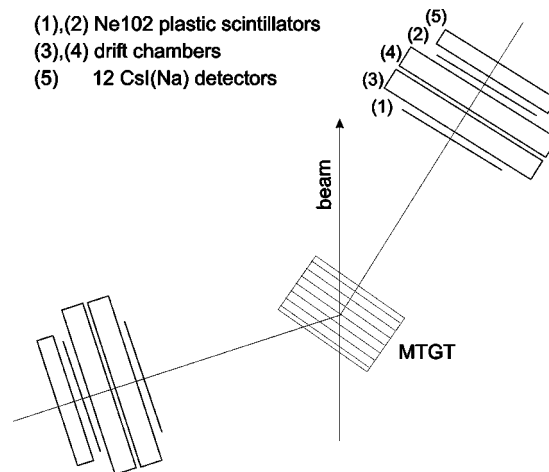


FIG. 4. Schematic view of SCANDAL setup.

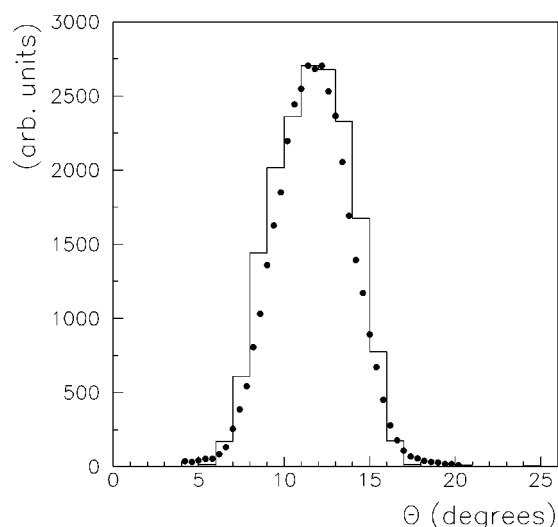


FIG. 5. Experimental distribution for emission angles of particles detected in a CsI detector (dots) compared with the simulation results (histogram).

Sec. III C, those events enabled us to apply an unambiguous normalization procedure for the extraction of the experimental cross sections, without requiring corrections for detection efficiencies, acquisition dead time, or beam intensity.

### III. DATA REDUCTION

The data recorded using both detection systems were analyzed on a event-by-event basis in order to extract the energy spectra of the emitted particles. The procedures used for each setup are described in the next two subsections. The last subsection is dedicated to the cross section normalization method.

#### A. Event sorting for SCANDAL setup

The first step in the data analysis was to identify the target where the emission occurred inside the MTGT system. It was derived from the signals given by the multiwire proportional counters located between the targets. Then the trajectories calculated with the drift chambers enable us to determine the emission angle of each particle. In this way, both a target and

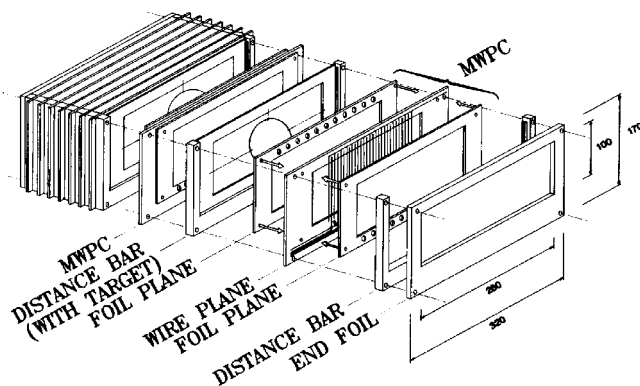


FIG. 6. Exploded view of the multitarget box.

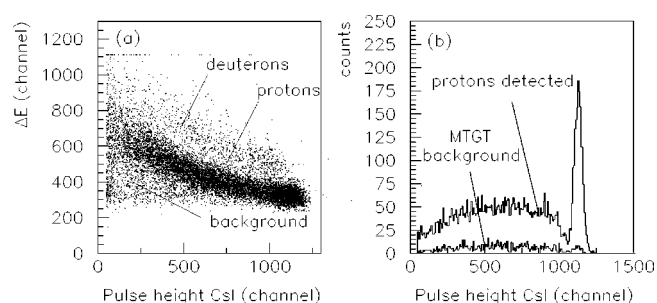


FIG. 7. (a) Two-dimensional scatter plot containing events recorded in the  $10^\circ$ – $11^\circ$  angular range using a  $\text{CH}_2$  target. (b) Contamination in the recorded proton spectra due to reactions in the multitarget box.

an emission angle are associated with each recorded event.

The particle identification was made by the well known  $\Delta E$ - $E$  technique, using signals from the plastic scintillators and the CsI detectors. An example of such an identification matrix is given in Fig. 7(a). It was obtained for the  $10^\circ$ – $11^\circ$  angular range, with a  $\text{CH}_2$  target. The small contribution of the deuterons that reached the CsI detectors, and a part of the background, were rejected by applying two-dimensional contours around the proton band. Another source of background that is present in the proton band was due to protons from nuclear reactions that occurred inside other multitarget box elements, different from the targets of interest. Mainly, they were protons arising from  $np$  scattering reactions in the cathode foils. That additional pollution had to be rejected with another technique that consisted of recording “blank-target” events with the MTGT emptied of targets. Subtraction of the corresponding spectra to those recorded during “physics” runs was performed after normalization to the same neutron fluency and to the same data acquisition dead time. Examples of proton spectra associated to blank-target runs and physics runs are shown in Fig. 7(b).

With the  $\text{CH}_2$  target, the energy calibration of the CsI detectors was done using protons produced in  $\text{H}(n,p)$  reactions, for which the emission energies could be accurately calculated. In order to reject the contribution from  $^{12}\text{C}(n,p)$  reactions, a pure carbon target was mounted together with the  $\text{CH}_2$  target inside the MTGT. Data on both targets were recorded simultaneously, so that, after normalization to the same number of carbon nuclei as in the  $\text{CH}_2$  target, events associated with  $^{12}\text{C}(n,p)$  reactions could be subtracted from the spectrum obtained with the  $\text{CH}_2$  target. Examples of spectra obtained with both targets are shown in Fig. 8, together with the proton spectrum resulting from the subtraction. The latter presents a peak and a tail, reflecting the incident neutron spectrum presented in Fig. 2. Both features correspond to  $\text{H}(n,p)$  events induced, respectively, by 96 MeV projectiles and by neutrons of lower energies contained in the beam tail. The proton energy spectra were obtained after calibration of the CsI detectors and corrections for energy losses inside the setup. These corrections were determined by Monte Carlo simulations for which attention has been paid to reproduce accurately the experimental conditions. The proton energy threshold equals 30 MeV. This large value is related to the long flight (about 84 cm) through of air and detector materials of the system.



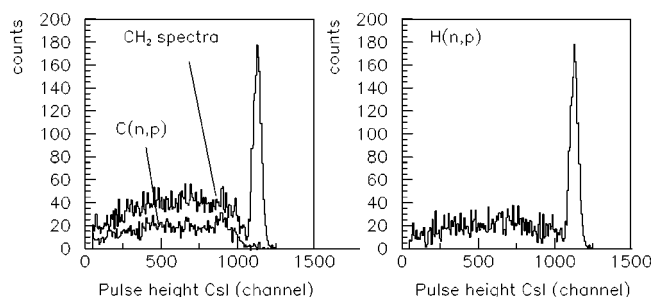


FIG. 8. Contribution of protons from the  $^{12}\text{C}(n,p)$  reaction in the  $\text{CH}_2$  spectra (left part). On the right, the spectra of protons from the  $\text{H}(n,p)$  elastic scattering obtained after subtraction are shown.

### B. Low-energy neutron rejection

In order to select only events induced by 96 MeV neutrons, the contribution of low energy neutrons had to be rejected. This has been done using a technique based on time-of-flight (TOF). The TOF values measured were the sum of the neutron TOF and the produced proton TOF. From the proton energy, the corresponding TOF can be calculated and subtracted from the total TOF measured. The result is the TOF of the neutrons that induced the reaction. In Fig. 9 are presented total time of flight, proton TOF, and neutron TOF spectra. The events associated with 96 MeV projectiles populate the peak centered at 78 nsec in the neutron TOF spectrum. This time corresponds to the experimental path of 1062.8 cm. A selection of that peak could then be easily applied.

In this way, spectra of protons from reactions induced by 96 MeV neutrons were constructed. In Fig. 10 two examples of such spectra obtained for  $\text{Pb}(n,Xp)$  and  $\text{H}(n,p)$  reactions recorded simultaneously with the MTGT system are presented. As it can be seen, for  $\text{H}(n,p)$  elastic scattering reactions, after selection, only the peak at high energy remains in the spectrum, compared to that of Fig. 8, while the contribution originating from low-energy neutrons has been completely removed. This is a confidence check of the time-of-flight method used for the event selection. The statistics accumulated in both spectra presented in Fig. 10 corresponds to about 2 h of acquisition time.

### C. Event sorting for MEDLEY setup

For the MEDLEY setup, the particle identification has been done using the well known  $\Delta E$ - $\Delta E$  and  $\Delta E$ - $E$  tech-

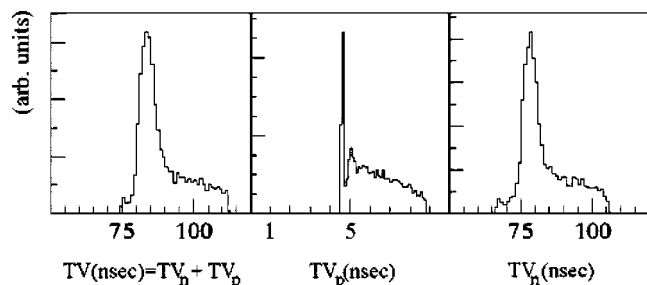


FIG. 9. Experimental determination of incident neutron time of flight.

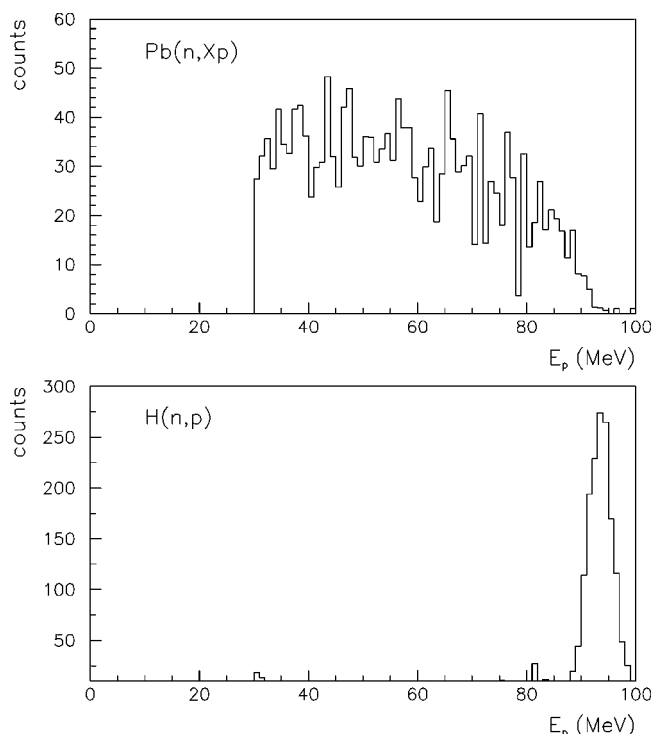


FIG. 10. Energy spectra of protons emitted in the angular range  $10^\circ$ – $11^\circ$  from neutron-induced reactions on a lead target (top) and from the elastic scattering reaction (bottom) at 96 MeV incident energy.

niques. Examples of two-dimensional plots obtained after energy calibration of each detector, for each particle type, are presented in Fig. 11. The top figure represents particles stopped inside the second silicon detector, while the lower one shows particles which reached the CsI scintillator.

For calibration purposes, the points where each particle type start to punch through the silicon detectors were used. The corresponding energies were calculated with the detector thickness given by the manufacturer and the stopping power data from Ref. [11]. In addition, for the thin silicon detectors, the calibration was checked using 5.48 MeV  $\alpha$  particles that stopped inside these detectors and that were emitted by a  $^{241}\text{Am}$  source. The energy deposited in the CsI(Tl) detectors has been further calculated for each particle type using the energy losses inside the silicon detectors. Supplementary calibration points in the case of protons were provided by the  $\text{H}(n,p)$  reactions on a  $\text{CH}_2$  target. These points provide a cross-check of the correctness of the assumed silicon detector thicknesses. Even a very small error in the thickness would make the two sources of information, i.e., the energies calculated from the peaks and from the energy loss in the  $\Delta E_1$  and  $\Delta E_2$  detectors incompatible. The method and the different parameterizations used are presented in detail in Ref. [8].

Finally, the total energy of each emitted particle is deduced by adding the different energies deposited inside the three individual detectors of each telescope. Figure 12 shows energy spectra of  $p$ ,  $d$ ,  $t$  and  $\alpha$  particles obtained from a lead target with the telescope placed at  $40^\circ$ . The arrows show the overlapping region between the second silicon and the CsI detector contributions.

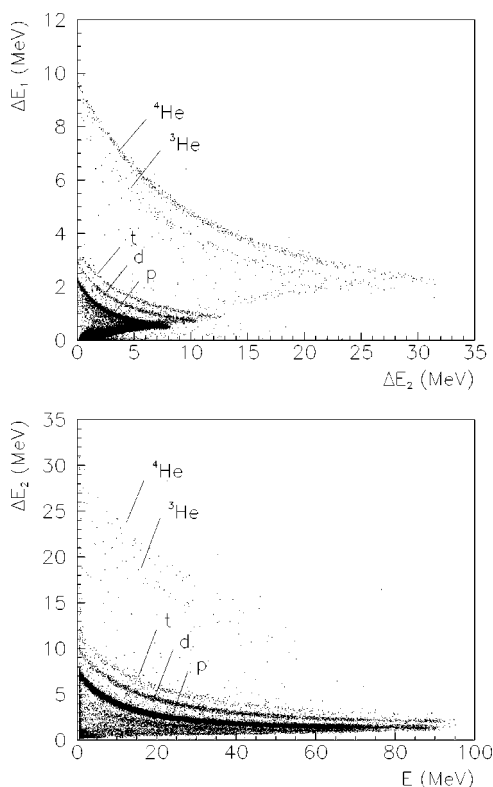


FIG. 11. Two-dimensional plots showing particles stopping in the second silicon detector (top) and in the CsI detector (bottom) of the telescope placed at  $40^\circ$  using a  $\text{CH}_2$  target.

The detection thresholds are given by the thickness of the first silicon detector. It is about 2–3 MeV for the hydrogen isotopes and about 9 MeV for the helium isotopes, as it can be seen in Fig. 11. The spectra had to be further corrected for

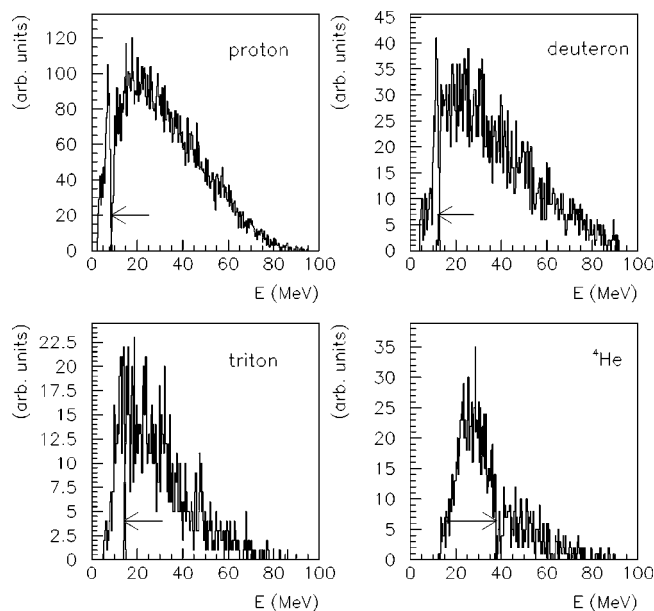


FIG. 12. Energy spectra for particles detected by the telescope placed at  $40^\circ$  with all neutrons from the beam incident on a lead target.

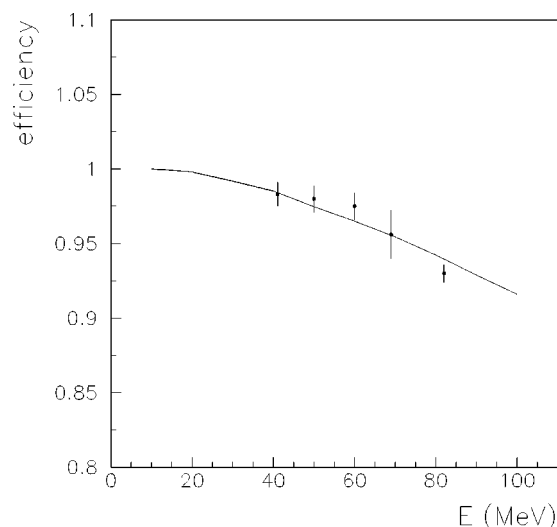


FIG. 13. Energy dependence of the CsI detection efficiency for protons. Simulation result (continuous line) is compared with the experimental values from Ref. [9].

the particle energy loss inside the emission target. Those corrections were calculated using Monte Carlo simulations, with targets of about  $50\ \mu\text{m}$  thickness. The maximum correction value estimated is less than 4 MeV, for low-energy  $\alpha$  particles. This shows that the corrections to be applied remain within reasonable limits.

The rejection of events associated with low-energy neutrons was done with the same procedure as for SCANDAL (Sec. III B). The background is dominated by protons arising from neutron-induced reactions inside the beam tube, at the entrance of the vacuum chamber. That contribution is subtracted by using the spectra accumulated during blank-target runs, applying a normalization to the same neutron fluency as for target-in runs, and taking into account corrections for the data acquisition dead time differences.

For the MEDLEY and SCANDAL setups, the CsI scintillator efficiency depends on the energy and type of the detected particle. Small corrections for the loss of light in the CsI detectors have then also to be applied. This effect is due to nuclear reactions that charged particles can undergo while slowing down inside the CsI. Corrections for this effect have been estimated for all charged particles, using reaction cross sections available in the GEANT library from CERNLIB [12]. Those estimations enable us to determine the CsI detector efficiency as presented in Fig. 13 for protons (continuous line). The loss of light inside the CsI detector is rather important for high energy protons and it is less pronounced for heavier particles. The detection efficiency at 100 MeV equals 91% for protons, 93% for deuterons, 95% for tritons, and 99% for  $\alpha$  particles and it increases as the energy decreases. As shown in the figure, simulation results are in very good agreement with the experimental values from Ref. [9].

#### D. Cross section normalization

Due to the difficulty encountered when monitoring a neutron beam intensity, the absolute cross section normalization

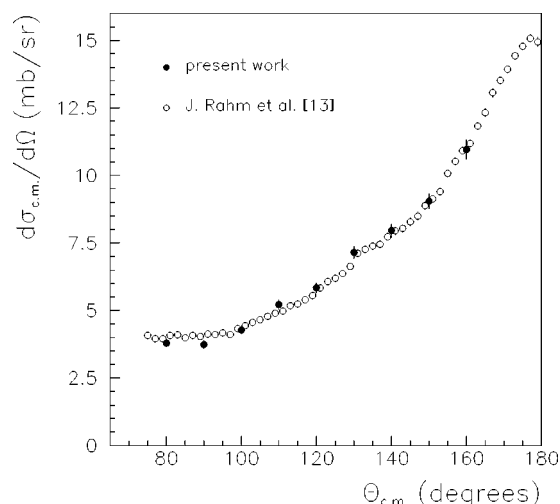


FIG. 14. Differential  $np$  scattering cross section at 96 MeV. The results obtained in the present work using the SCANDAL setup are compared to the data from Ref. [13].

in neutron-induced reactions is a notorious problem. In particular for our experiments, the uncertainty affecting the value given by the fission monitor equals 10%, which induces large uncertainties for the values of the measured cross sections. Therefore, the cross sections are measured relative to another one, considered as a reference. The reference cross section most often used is the  $H(n,p)$  cross section, for which a recent measurement claims an absolute uncertainty of 2% [13]. We have used the values given in that reference to calculate the absolute cross sections. Nevertheless, in order to be able to apply the normalization procedure, we have to measure in the same experimental conditions the number of protons emitted in  $H(n,p)$  reactions because that number intervenes in the normalization factor. When measuring that number, we took the opportunity to remeasure the angular distribution of the  $H(n,p)$  cross section.

For that purpose, we used the SCANDAL setup. We determined the number of recoiling protons after subtraction of the  $^{12}\text{C}(n,p)$  reaction component and the background contribution, following the procedure presented in Sec. III A. The angular range being limited in our measurements to  $80^\circ$ – $160^\circ$  for neutrons in the center of mass system, we extracted values for the other angles by fitting our data with a fourth-order Legendre polynomial. Then, considering other channels negligible at 96 MeV, we normalized the value of the deduced total  $np$  cross section to that given in Ref. [14]. Finally, we obtained the angular distribution, which is presented in Fig. 14 together with the experimental results of Ref. [13]. We observe a very good agreement between both. However, the uncertainties of the cross sections from Ref. [13] are significantly smaller than those in our experiment (2%). Indeed, for our data, the statistical errors are typically in the range 1.5–2.8 %, and the total uncertainty is estimated of the order of 4.1%, including the 1% contribution from the total  $np$  cross section [14]. The systematical errors affecting our results arise from the subtraction of reactions on carbon, from the integration over the  $np$  peak, and from the rejection of events induced by low-energy neutrons.

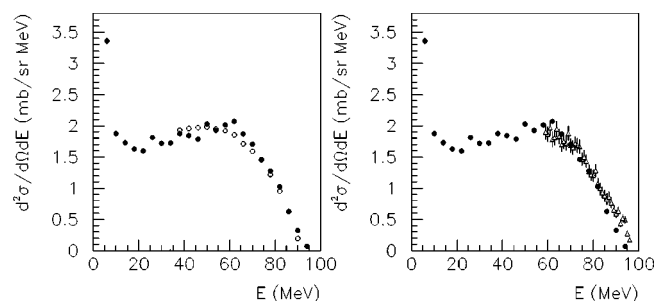


FIG. 15. Left panel:  $\text{Fe}(n,Xp)$  double-differential cross sections measured with MEDLEY setup at  $\theta=20^\circ$  (full circles), compared to the SCANDAL results (open circles). Right panel: same data compared to those from Ref. [15] (open triangles).

For the SCANDAL setup, the MTGT system was used to measure at the same time protons emitted from the target under study (iron, lead, or uranium) and in  $H(n,p)$  reaction from the  $\text{CH}_2$  target. The normalization procedure could then be applied without precise knowledge of the neutron flux. For the MEDLEY setup, all data have been normalized using the  $H(n,p)$  scattering peak recorded by the telescope placed at  $20^\circ$  during separate runs with a  $\text{CH}_2$  target.

For the proton emission, data recorded using the SCANDAL and MEDLEY setups were individually normalized, allowing two independent determinations of the cross sections for all targets studied. With this procedure, the estimated systematical uncertainties of the experimental cross sections are not greater than 5.1%. To calculate this value, we took into account the contributions from the number of target nuclei (2%), the solid angles calculated by simulations (0.75%), the beam monitor stability during the data taking (2%), the number of recoiling protons from the  $np$  reaction (3.7%), and the reference  $np$  cross sections (2%) according to Ref. [13].

#### IV. EXPERIMENTAL RESULTS

The double-differential cross sections of light charged particles were measured for three targets, Fe, Pb, U, with natural isotopic compositions, over an angular range of  $20^\circ$ – $160^\circ$ . For the MEDLEY setup, the low energy threshold was 4 MeV for hydrogen isotopes, 12 MeV for  $^3\text{He}$ , and 8 MeV for  $\alpha$  particles. For the SCANDAL setup, it was 35 MeV for protons. Due to the detector energy resolution and the available accumulated statistics, a 4 MeV bin size has been chosen for the energy spectra.

In the left part of Fig. 15, proton double-differential cross sections measured independently with the MEDLEY setup (full circles) and with the SCANDAL setup (open circles) are compared. The spectra correspond to the Fe target and a  $20^\circ$  emission angle. Over the energy range covered by both detection devices, we observe a very good agreement. This shows that the systematical uncertainties induced by the cross section normalization are small. We obtained similar results for the other targets (Pb and U) and over the full angular range. In addition, it shows that the limited angular resolution of MEDLEY does not distort the distributions that

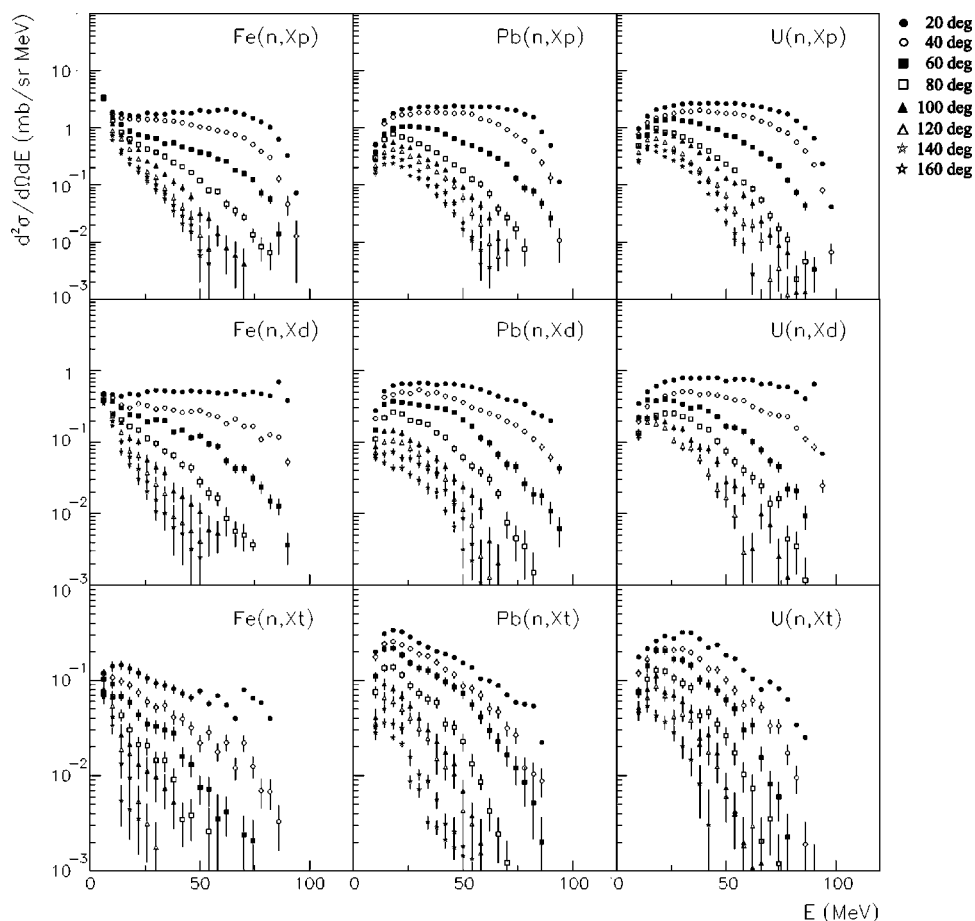


FIG. 16. Double-differential cross sections for  $p$ ,  $d$ , and  $t$  (top, middle, bottom lines, respectively) produced in 96 MeV neutron-induced reactions on Fe, Pb, and U targets (left, middle, and right rows, respectively).

are comparable to that obtained with SCANDAL, for which the angular resolution is much better. The right part of Fig. 15 gives a comparison of the  $\text{Fe}(n,Xp)$  cross section measured at  $20^\circ$  with MEDLEY, with the data from Ref. [15] that were obtained using the magnetic spectrometer LISA. Very good agreement is found also between these two measurements. This shows the quality of our measurements and of the data analysis procedures employed. We observed a similar agreement for the  $\text{Pb}(n,Xp)$  cross sections.

In Fig. 16 are presented experimental double-differential cross sections for  $p$ ,  $d$ ,  $t$  (top, middle, bottom lines, respectively) produced in 96 MeV neutron-induced reactions on Fe, Pb, and U targets (left, middle, and right rows, respectively) and measured with the MEDLEY setup. In Fig. 17, for the same reactions, we report the complementary production cross sections of  $^3\text{He}$  and  $\alpha$  particles (top and bottom figures, respectively). The errors shown are purely statistical.

The general trend observed is a decreasing emission probability with increasing angle, over the full energy range. The angular distributions are slightly forward peaked at low energies, and at backward angles the emission probabilities are very low for energetic particles. In the case of the iron target, a quasi-isotropic component is observed at very low energy (0–10 MeV). This contribution is not present for heavier targets, for which Coulomb effects are much larger. For the rest of the energy range, the distributions obtained with the three targets are very similar in shape. For  $^3\text{He}$  particles, distributions have been measured only for the iron target.

Despite the long data acquisition time, no corresponding events were recorded for the other targets. This is related to the very low  $^3\text{He}$  emission probability for heavy targets, which has been already observed in Ref. [16], where the  $^3\text{He}$  production rate in 63 MeV proton-induced reactions on  $^{208}\text{Pb}$  is about 10 times smaller than that for tritons.

For a more detailed analysis of the particle emission mechanisms, a separate inspection of angular and energy-differential distributions is needed. The angular distributions were obtained from double-differential cross sections by integration over the full energy range. For the energy distributions, we used the Kalbach systematics [17] in order to extrapolate the experimentally available angular range over the entire space. This can be done very accurately since the systematics described in Ref. [17] has been established using data measured in the same angular domain as in our experiments. Finally, the total production cross sections were derived for each particle type by integrating the corresponding energy-differential cross sections over the experimental energy range.

The energy-differential cross sections are presented in Fig. 18 for the iron and lead targets. The results obtained with the uranium target are very similar to those extracted for the lead one. By analyzing the spectra, we distinguish two regions. For energies greater than about 20 MeV, proton and deuteron spectra are very similar in shape, the emission probability decreasing slowly with energy for both targets. In the case of the iron target, the triton and  $^3\text{He}$  spectra also show a similar behavior. For  $\alpha$  particles, the spectra decrease very



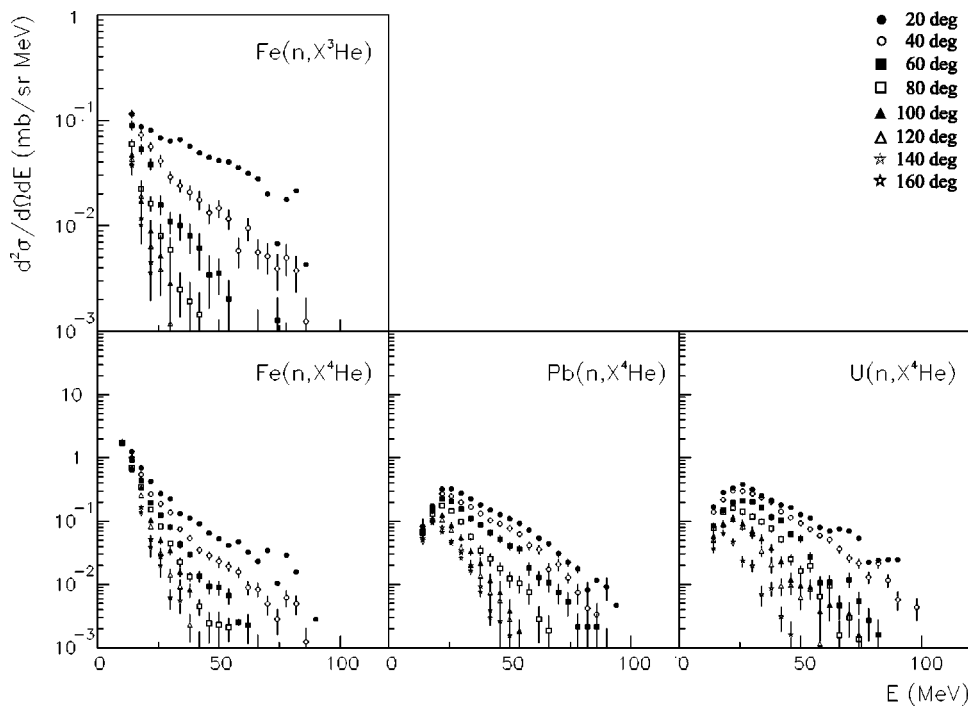


FIG. 17. Same as Fig. 16 for helium isotopes

rapidly with energy. For a given particle, the shapes of the iron and lead distributions are very similar. In this energy region, the emission probability distributions have steeper slopes for heavy particles than for light ones. Another important aspect to be noticed is the decreasing emission probability with the nucleon number of the emitted particle. However, an exception is observed for  $\alpha$  particles for which the production cross sections in the low-energy part of the continuum region ( $20 \text{ MeV} < E < 35 \text{ MeV}$ ) are larger than those for tritons, suggesting a more complex mechanism for their

emission. For low emission energies ( $E < 20 \text{ MeV}$ ), a dominant contribution is observed for all particles in the case of the iron target. The shape of the distributions in Fig. 18, correlated to the slow variation of the amplitude with the emission angle observed in Figs. 16 and 17, suggests that these low energy particles are emitted mainly during the evaporation process of an excited nucleus. This component is not present in the spectra obtained with the lead and uranium targets because, for heavy targets, the emission of low-energy particles is strongly inhibited by Coulomb effects. This explains the low cross sections found in this energy range for both lead and uranium targets.

Figure 19 shows the angular distributions obtained by integrating double-differential distributions. Due to the detection thresholds, the integration domains range over 4–96 MeV for hydrogen isotopes, 12–96 MeV for  $^3\text{He}$ , and 8–96 MeV for  $\alpha$  particles. For all particles, the distributions are strongly forward peaked, suggesting that nonequilibrium processes are dominant for the reactions under study. An exception can be noticed for  $\alpha$  particles in  $\text{Fe}(n,X)$  reactions, where the distribution is almost flat for angles larger than  $50^\circ$ . This suggests that the emission of  $\alpha$  particles in the backward hemisphere could result mainly from evaporation processes. For a given particle, the angular distributions are more forward peaked for the heavier nuclei, suggesting that the nonequilibrium component increases with the nucleon number of the target.

This can also be observed from Table I, where integrated total cross sections (second column) and integrated nonequilibrium cross sections (third column) are presented as a function of the target mass, for all particles. Depending on the system considered, the nonequilibrium cross sections were extracted with different methods. For the  $\text{Fe}(n,X\text{lcp})$  reactions (lcp refers to light charged particles), the low-energy contribution in the energy-differential cross sections (Fig.

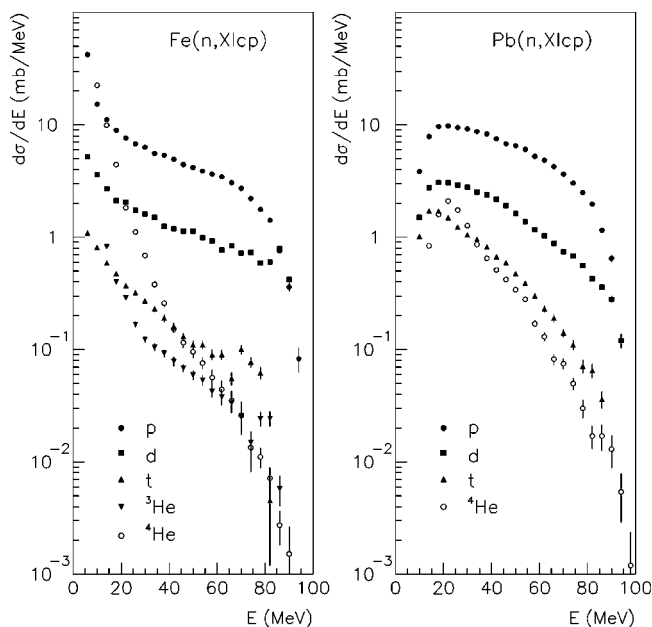


FIG. 18. Energy distributions for light charged particles produced in the 96 MeV neutron-induced reaction on iron and lead targets (left and right panels, respectively).

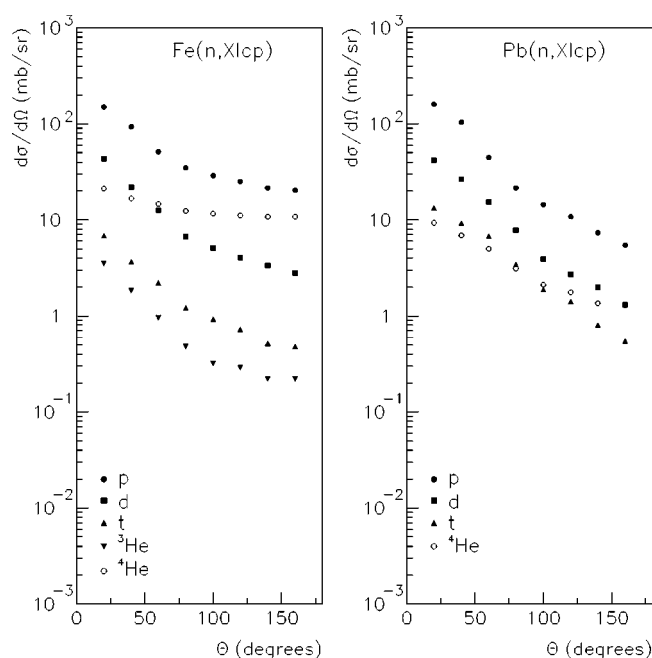


FIG. 19. Angular distributions for light charged particles produced in the 96 MeV neutron-induced reaction on iron and lead targets (left and right panels, respectively).

18) was fitted with an exponential function and its integral was then subtracted from the total cross section for each particle. For lead and uranium targets, we made the assumption that all particles were emitted during nonequilibrium processes, i.e., in a first approximation, the rather small contribution of evaporated particles expected at low energy is neglected.

The values from Table I show that for all targets studied, more than 30% of the total light-charged-particle production are particles heavier than protons. This is an important aspect

TABLE I. Total light-charged-particle integral cross sections and estimated contributions from the nonequilibrium emission in neutron-induced reactions at 96 MeV.

Reaction	Total cross section (mb)	Non-equilibrium cross section (mb)
Fe( <i>n</i> , <i>Xp</i> )	584±29.2	326
Pb( <i>n</i> , <i>Xp</i> )	485±24.3	485
U( <i>n</i> , <i>Xp</i> )	589±29.5	589
Fe( <i>n</i> , <i>Xd</i> )	131±6.5	96
Pb( <i>n</i> , <i>Xd</i> )	137±6.9	137
U( <i>n</i> , <i>Xd</i> )	170±8.5	170
Fe( <i>n</i> , <i>Xt</i> )	21±1.1	15
Pb( <i>n</i> , <i>Xt</i> )	53±2.7	53
U( <i>n</i> , <i>Xt</i> )	54±2.8	54
Fe( <i>n</i> , <i>X</i> <sup>3</sup> He)	10±0.5	7
Fe( <i>n</i> , <i>X</i> <sup>4</sup> He)	167±8.3	31
Pb( <i>n</i> , <i>X</i> <sup>4</sup> He)	45±2.2	45
U( <i>n</i> , <i>X</i> <sup>4</sup> He)	52±2.6	52

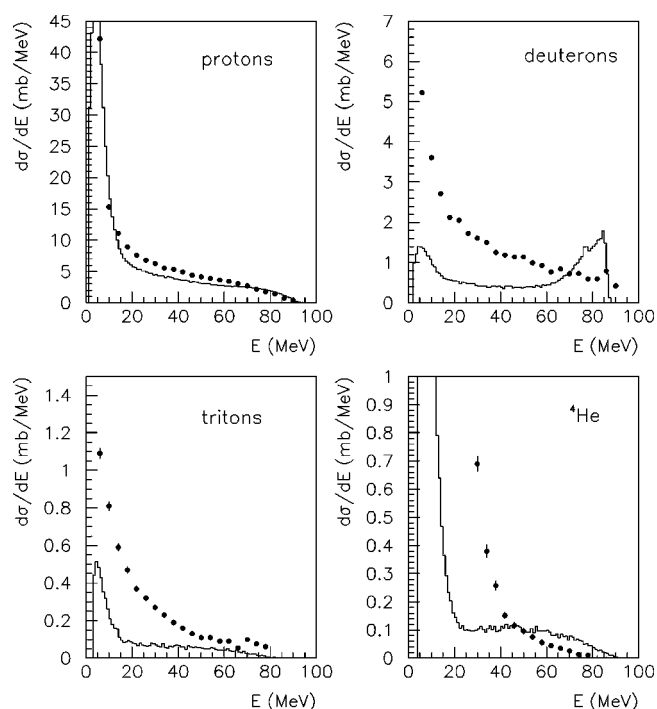


FIG. 20. Energy-differential cross sections calculated using the GNASH code for the <sup>56</sup>Fe(*n*,*Xlcp*) reaction at 96 MeV (histograms) compared with the present experimental results (points).

to be pointed out, because, with such a production rate, the contribution of these particles should not be neglected.

## V. THEORETICAL CALCULATIONS

At this moment, the exciton model [2] is the most commonly used to calculate the preequilibrium emission in nucleon-induced reactions at intermediate energies. This model assumes that the excitation process takes place by successive nucleon-nucleon interactions inside the nucleus. Each interaction produces another exciton, leading the system to the final state of statistical equilibrium through more complex states. Occasionally a particle can receive enough energy to leave the system and subsequently be emitted. The resulting preequilibrium spectrum is the sum of the contribution from each state. Particles emitted in the early stages have more energy than those emitted in the later ones. In the framework of this model, only energy distributions of emitted particles can be calculated.

The GNASH code [6] is one example that uses the exciton model to calculate the preequilibrium component. It is able to calculate spectra for nucleons and complex particles. In this code, the equilibrium contribution is calculated using the Hauser-Feshbach formalism [18]. Cross sections that were evaluated with GNASH are at present implemented in MCNPX, a code widely used for specific applications such as medical or engineering studies. In Figs. 20 and 21, we compare, respectively, the <sup>56</sup>Fe(*n*,*Xlcp*) and <sup>208</sup>Pb(*n*,*Xlcp*) energy-differential cross sections of the present work (points) to the GNASH predictions (histograms) obtained with MCNPX. The maximum value in the  $\alpha$ -particle spectrum for the iron target

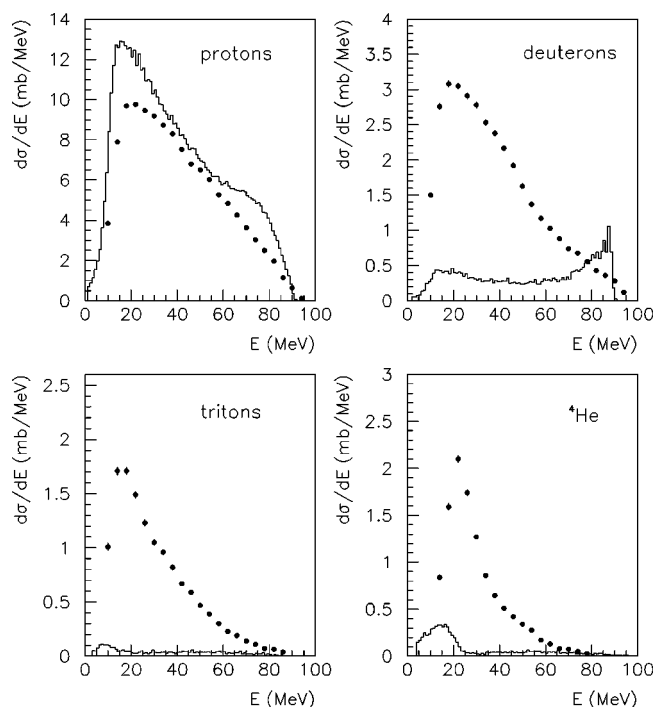


FIG. 21. Same as in Fig. 20 for the  $^{208}\text{Pb}(n, \text{Xlcp})$  reaction.

has been set to 1 mb/MeV for better visualization. While the proton emission is relatively well described, we observe that the production of complex particles is strongly underestimated.

This comparison suggests that significant improvements are needed in the original exciton model in order to increase its prediction level concerning the cluster emission. To modify it according to this request, a first approach was proposed in 1973 by Ribanský and Obložinský [3]. It introduces the probability of a cluster formation during the nucleon-nucleon interactions inside the target. In 1977, Kalbach formulated a second approach [4], which includes contributions from direct pick-up and knock-out mechanisms. Both approaches have been tested in the past against data and they lead to a satisfactory agreement with the experimental results [4,5], despite their completely different basic assumptions. Nevertheless, conclusions about their global predictive power were limited, mainly because a restricted number of experimental results were available at that moment. In order to get a wider view on their predictive capabilities, we performed calculations with both approaches for the  $^{56}\text{Fe}(n, \text{Xlcp})$ ,  $^{208}\text{Pb}(n, \text{Xlcp})$ ,  $^{238}\text{U}(n, \text{Xlcp})$  reactions at 96 MeV, but also for other projectiles, at different incident energies and for other targets, for which experimental data are available in the literature. In the following, we will give a basic description of both approaches and discuss the comparisons of the calculations with a set of data that cover a wide domain of reaction entrance-channel parameters.

#### A. Cluster formation probability in nucleon-nucleus reactions

Difficulties were encountered in the original exciton model proposed by Griffin to reproduce the experimental

distributions of complex particles, which was then modified first by Ribanský and Obložinský [3]. The modification consists of the introduction in the particle production rate expression of a multiplicative term containing the cluster formation probability  $\gamma_\beta$  where  $\beta$  is the type of the emitted particle. The physical meaning of this parameter has been given in Ref. [19] in the framework of the coalescence model. This approach assumes that complex particles are formed during the preequilibrium stage from excited nucleons that share the same volume in the momentum space. In this way, for example, an excited proton and an excited neutron can coalesce into a deuteron if the transverse momentum between both is small. The drawback of this approach is its limited predictive power since the parameter  $\gamma_\beta$  has to be adjusted in order to reproduce as well as possible the amplitude of the experimental energy-differential distribution under study. Nevertheless, it is always interesting to compare the tuned results of a model with experimental data.

The formation probability  $\gamma_\beta$  of a complex particle  $\beta$  is given as a function of the radius of the coalescence sphere  $P_0$  in the momentum space by the formula:

$$\gamma_\beta = \left| \frac{4}{3} \pi (P_0/mc)^3 \right|^{p_\beta-1}, \quad (1)$$

where  $p_\beta$  is the number of nucleons of the emitted particle. Of course,  $\gamma_\beta=1$  in the case of the emission of a nucleon. According to Eq. (1),  $\gamma_\beta$  and thus,  $P_0$  are the free parameters of the model.

The following expression for the cluster formation probability has been proposed in Ref. [20]:

$$\gamma_\beta = (p_\beta)^3 (p_\beta/A)^{p_\beta-1}, \quad (2)$$

where  $A$  is the mass of the target nucleus. This approach is implemented in the latest version of the code GEANT [21], which is intensively used for simulations among the physics community. However, calculations from Ref. [20] strongly overestimates deuteron, triton and  $^3\text{He}$  distributions, while the production rates for  $\alpha$  particles are underestimated. This shows that the calculation of the cluster formation probability according to Eq. (2) is not very appropriate. For this reason, calculations in this work have been done with the PREEQ program [22], keeping the cluster formation probability as a free parameter. A complete explanation about the different parameters of the model and the method we applied to calculate them can be found in Ref. [5]. In the forthcoming discussion, we will focus onto the cluster formation probability  $\gamma_\beta$  because of its particular importance for the model predictions.

In the first step of our investigation, we performed calculations with PREEQ for the 96 MeV neutron-induced reactions presented in this work. We determined two sets of values for the  $\gamma_\beta$  parameter by normalizing individually the calculated energy distributions to the  $\text{Fe}(n, X)$  and  $\text{Pb}(n, X)$  experimental data. For those reactions, PREEQ results (histograms) and data (points) are presented in Fig. 22 for  $^{56}\text{Fe}$  and  $^{208}\text{Pb}$  targets. We have to remind readers that the model calculates only the preequilibrium component of the emission spectra, so that in our comparison, we should not consider either the low-energy region populated with particles evaporated by excited nuclei or the high-energy region where di-

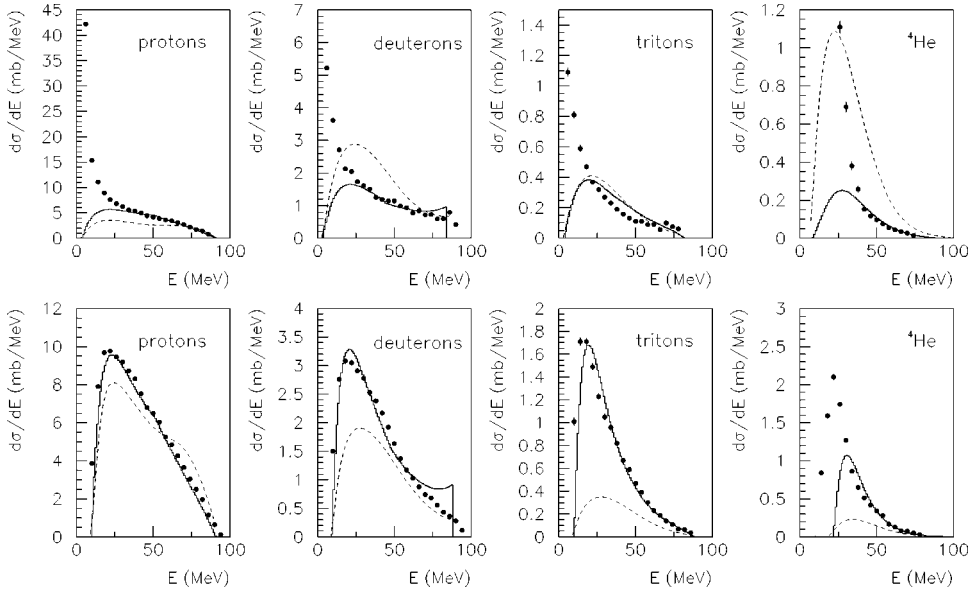


FIG. 22. Energy-differential cross sections calculated using PREEQ (histograms) and PRECO-2000 (dashed line) for  $^{56}\text{Fe}(n, X)_{\text{cp}}$  (top) and  $^{208}\text{Pb}(n, X)_{\text{cp}}$  (bottom) reaction at 96 MeV, compared with the experimental results of the present work (points). Maximum value in the plotting scale for the  $\alpha$  particle in the case of the iron target has been set to 1.2 mb/MeV for a better visualization.

rect reactions are supposed to be dominant. Considering those restrictions, we observe that the shapes of the calculated distributions are in good agreement with the experimental results. As expected, the model fails in reproducing the very-low-energy component of the iron spectra. For all particles in the  $^{208}\text{Pb}(n, X)$  reactions, except  $\alpha$  particles, the calculated preequilibrium contribution accounts for almost the entire energy range, showing that almost all particles are emitted during the preequilibrium stage. For  $\alpha$  particles, the preequilibrium processes are still underestimated by PREEQ in the low-energy region of the continuum. By comparison with the GNASH predictions presented in Figs. 20 and 21, we clearly see that this approach improves dramatically the original exciton model, for all particles.

For protons, for which the  $\gamma_\beta$  parameter equals 1 and does not need to be adjusted, the amplitudes of the distributions are very well described by the model in the energy range where it is applicable. It must be pointed out that only the

primary preequilibrium contribution is calculated by this code. The good agreement found for protons suggests that the second-chance preequilibrium component is very small, in agreement with the calculations from Ref. [23]. For complex particles, no conclusion about the predictive capabilities of PREEQ can be drawn at the moment, the amplitude of the distributions being obtained by adjusting the  $\gamma_\beta$  parameter in order to get good agreement with the experimental data. Therefore, the next step in our analysis was to check the stability of this parameter while changing the entrance channel, i.e., the incident energy and the projectile, for a target nucleus in the mass region  $A=208$ . For that aim, using the values of the cluster formation probabilities previously obtained for the 96 MeV  $^{208}\text{Pb}(n, X)$  reactions, we calculated the energy-differential cross sections for 39 MeV  $^{209}\text{Bi}(p, X)$  and 63 MeV  $^{208}\text{Pb}(p, X)$  reactions. In Fig. 23, the resulting PREEQ calculations (histograms) are compared with the experimental data (points) measured at 39 MeV with a  $^{209}\text{Bi}$

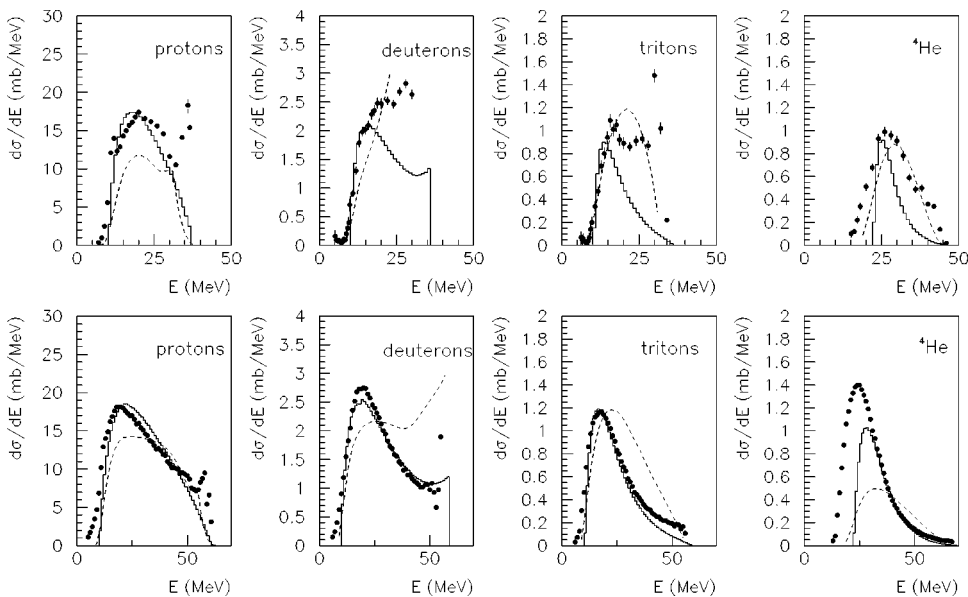


FIG. 23. Energy-differential cross sections calculated using PREEQ (histograms) and PRECO-2000 (dashed line) for  $^{209}\text{Bi}(p, X)_{\text{cp}}$  reactions at 39 MeV (top) and  $^{208}\text{Pb}(p, X)_{\text{cp}}$  reactions at 63 MeV (bottom), compared with the experimental results from Refs. [24,16] (points).



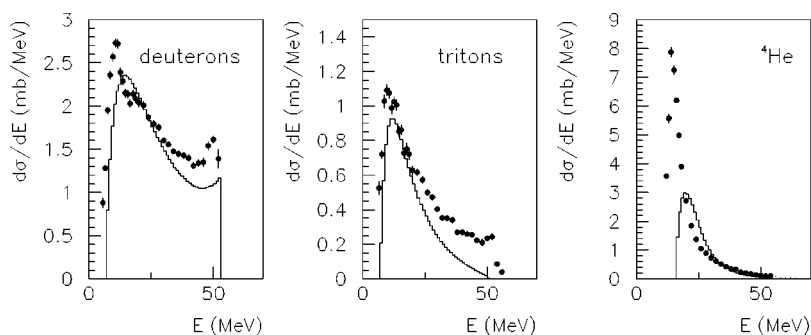


FIG. 24. Energy-differential cross sections calculated using the PREEQ code (histograms) for  $^{120}\text{Sn}(p, Xlcp)$  reaction at 62 MeV compared with the experimental results from Ref. [24] (points).

target [24] (top panels) and to the data measured at 63 MeV with the  $^{208}\text{Pb}$  target [16] (bottom panels). Over the energy domain where the model is applicable, we observe again a good agreement between the calculations and the experimental results. In addition and especially at 39 MeV, we see that the noncalculated direct process contribution is dominant.

From this study, we conclude that the free parameter  $\gamma_\beta$  depends neither on the projectile type (neutron or proton) nor on the incident energy and that, once the cluster formation probability has been adjusted to the reaction system, the model has a good predictive power for reactions with the same target. To go further, we have now to investigate its possible dependence with the target mass. Since we have just determined the formation probability  $\gamma_\beta$  for two target nuclei with masses  $A=56$  and  $A=208$ , we choose an intermediate target with a mass  $A=120$  for which experimental data were measured, i.e., the  $^{120}\text{Sn}(p, Xlcp)$  reaction at 62 MeV incident energy [24]. With the same method described previously, we calculated the new set of  $\gamma_\beta$  values associated to the  $^{120}\text{Sn}$  target. In Fig. 24, we compare the corresponding PREEQ calculations (histograms) to the data (points). As for the other targets, we observe the same global good reproduction of the data in the preequilibrium energy region.

In Table II, we gather the values of the cluster formation probabilities, as well as the related  $P_0$  parameters, obtained for the three target nuclei  $A=56$ ,  $A=120$ , and  $A=208$  and for each complex particle type. The formation probability for each particle type is also represented as a function of the target mass in Fig. 25.

TABLE II. Cluster formation probability in nucleon-induced reactions on three targets and corresponding radii of the coalescence sphere in the momentum space.

Target	Emitted particle	Formation probability $\gamma_\beta$	$P_0$ (MeV/c)
$^{56}\text{Fe}$	$d$	0.0278	175
	$t$	0.0065	250
	$^3\text{He}$	0.0060	246
	$^4\text{He}$	0.0052	322
$^{120}\text{Sn}$	$d$	0.0230	164
	$t$	0.0050	238
	$^4\text{He}$	0.0035	304
$^{208}\text{Pb}$	$d$	0.0186	153
	$t$	0.0035	225
	$^4\text{He}$	0.0018	286

We observe that for a given particle, the formation probability and then the coalescence sphere radii are smaller for heavier nuclei. Under the assumption of phase space relations, a smaller  $P_0$  value means a larger volume inside the nucleus from which the particle is emitted. This volume is then larger for heavier nuclei. In addition, for a given target nucleus, the figure shows that the formation probability decreases as the number of nucleons of the emitted particle increases. This could be explained by the fact that it is less probable, for example, for three nucleons to coalesce in order to form a triton, than for two nucleons to form a deuteron. The formation probability of deuterons is much larger than that for other complex particles, suggesting that the most probable mechanism is the pick-up of one nucleon by another.

The presently obtained values are in rather strong disagreement with those from Ref. [20]. Thus, for the  $^{208}\text{Pb}(p, Xlcp)$  reaction, the  $\gamma_\beta$  probability calculated according to Eq. (2) is 0.077 for deuterons, 0.0056 for tritons, and 0.00046 for  $\alpha$  particles. As it can be observed, the values for hydrogen isotopes are larger than those obtained in this work, leading to the overestimation found in Ref. [20] for the production of these particles. On the other hand, the values for  $\alpha$  particles are smaller than ours and thus the distributions calculated in Ref. [20] are systematically below the experimental results.

Another interesting aspect to point out is that the presented  $P_0$  values obtained for nucleon-nucleus reactions are

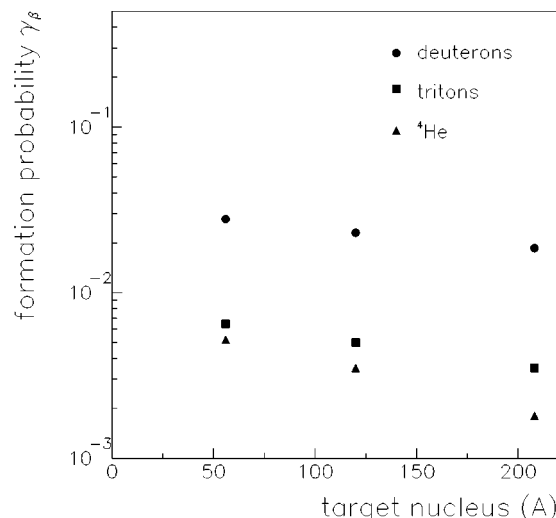


FIG. 25. Formation probability for each complex particle versus target mass.

in the same range as those extracted for reactions induced by complex projectiles (deuterons,  $^3\text{He}$ , and  $\alpha$  particles) at intermediate energies [25] and for reactions induced by heavy ions at high energies [26,27]. This suggests a weak dependence of this parameter with the projectile mass and energy.

To conclude, compared to the original exciton model existing in the GNASH code, the approach proposed by Ribanský and Obložinský and implemented in the PREEQ code improves greatly the predictions concerning complex particle production rates in preequilibrium processes, with the adjustment of one free parameter depending only on the target mass.

### B. Exciton model and direct reactions

In order to modify the original exciton model concerning the complex particle emission in nucleon-induced reactions, a completely different approach has been proposed by Kalbach [4]. It is based on the fact that direct reactions such as the nucleon pick-up process and the cluster knock-out process are not included inside the exciton model. Therefore this approach calculates their associated contributions separately and adds them to the preequilibrium component calculated with the original exciton model. Contrarily to the PREEQ program, this approach does not use any multiplication factor in the particle production rate expression, and thus it has no adjustable parameter. In other words, this approach proposes to replace the cluster formation probability introduced in Ref. [3] by the contribution of direct reactions. This modification is taken into account in the code PRECO-2000 [28] that calculates nucleon and complex particle nonequilibrium spectra in nucleon-induced reactions using (i) the two-component version of the exciton model and (ii) phenomenological models for direct reaction processes. This code is open to the community via the Data Bank Computer Program Services of the NEA. The same approach has been recently implemented in the TALYS code [29], which is still under development and therefore not yet available to the community.

Calculations have been done with the PRECO-2000 code using the set of global parameters recommended by the author for the contribution of direct processes. Details can be found in Ref. [28]. For the exciton model contribution, the same values for specific parameter as for the PREEQ calculations have been used. In Fig. 26 an example of the PRECO-2000 results obtained for the  $\alpha$ -particle emission in  $^{56}\text{Fe}(n,X)$  reactions at 96 MeV is given. The three individual contributions in the nonequilibrium spectrum are displayed. We observe that the very low contribution of the preequilibrium processes predicted by the exciton model (dash-dotted line) is compensated by the other two direct processes now included, i.e., the pick-up of three nucleons (dashed line) and the knock-out of  $\alpha$  particles (dotted line), which are assumed to be preformed inside the nucleus. The total nonequilibrium spectrum is obtained by summing all these contributions.

Following the same procedure as in the Sec. V A, calculations have been performed first for the data that we measured at 96 MeV. The results are presented in Fig. 22 for the  $^{56}\text{Fe}(n,X\text{lcp})$  and  $^{208}\text{Pb}(n,X\text{lcp})$  reactions (dashed lines). The

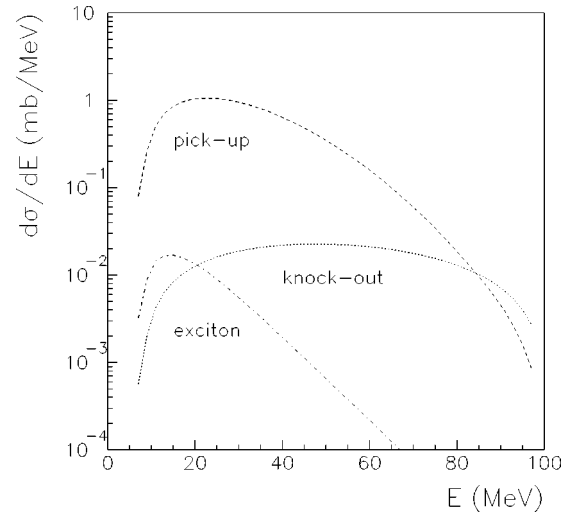


FIG. 26. Different mechanism contributions in the nonequilibrium  $\alpha$ -particle spectrum calculated using the PRECO-2000 code for the  $^{56}\text{Fe}(n,X)$  reaction at 96 MeV.

disagreement with the experimental distributions is rather strong for both systems. For the iron case, the nonequilibrium complex particle production is overestimated while the proton emission is underestimated. For the lead target, composite ejectile rates are underestimated, as well as the proton distribution. In addition, for a given target, the disagreement seems to become more important as the mass of the emitted particle increases. Even if the model in PRECO-2000 code predicts more particles in the preequilibrium region than GNASH does, experimental shapes and amplitudes are not as well reproduced as with the PREEQ code. In the case of nucleon ejectiles, the secondary preequilibrium emission can be considered in this code. However, this contribution was not included in the calculated spectra in order to get the same calculation conditions as in Sec. V A. This can explain the underestimation found for energies around 20 MeV in the proton spectra.

Despite its bad data reproduction observed at 96 MeV, we tested PRECO-2000 again by changing the incident particle and energy of the entrance channel. Doing so, we found a better agreement as it can be seen in Fig. 23, where the predictions of the PRECO-2000 code (dashed lines) for the 39 MeV  $^{209}\text{Bi}(p,X\text{lcp})$  (top panels) and the 63 MeV  $^{208}\text{Pb}(p,X\text{lcp})$  (bottom panels) reactions are compared to the experimental results from the Refs. [24,16] (points). Even if a tremendous disagreement still exists at low incident energies, the model predictions are sensibly improved with proton projectiles compared to those related to incident neutrons at 96 MeV. This suggests that the PRECO-2000 predictions strongly depend on the incident energy and the projectile type. That latter aspect can be studied in more detail since data with both neutron and proton projectiles are available for  $^{208}\text{Pb}$  at the same incident energy (63 MeV). In Fig. 27, are presented the experimental energy distributions of deuterons for both reaction types (top left panel): (i)  $(p,xd)$  [16] (open circles), and (ii)  $(n,xd)$  [30] (full circles). The experimental results are very similar in shape and in amplitude for both projectiles. The corresponding PRECO-2000 calculated distributions are

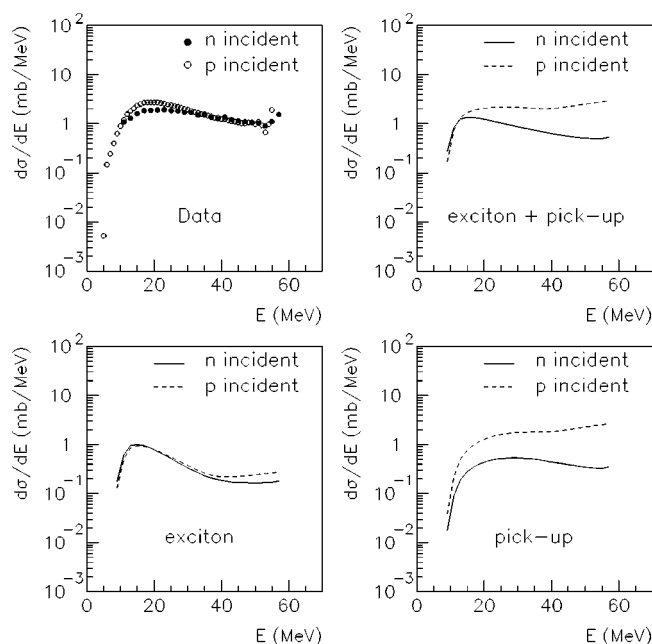


FIG. 27. Deuteron emission in proton- and neutron-induced reactions on  $^{208}\text{Pb}$  at 63 MeV. Experimental results (top left panel) are compared to the distributions calculated using PRECO-2000 code (top right panel). Contributions from preequilibrium (exciton model) (left bottom panel) and nucleon pick-up reaction (bottom right panel) are presented.

shown in the top right panel. As it can be seen, the theoretical distributions are very different when changing the incident nucleon type (neutron or proton), in a strong contradiction with the data. This disagreement does not originate from the preequilibrium contributions calculated by the exciton model because we checked that the corresponding distributions are similar for neutron- and proton-induced reactions (bottom left panel). On the other hand, the calculated contributions for the nucleon pick-up process (right bottom panel) are very different from each other and, since this mechanism is dominant, this difference generates the disagreement observed with the data. To conclude, the contribution of direct reactions as calculated in PRECO-2000 strongly depends on the incident particle type, contrary to the experimental data. This effect constitutes, of course, a shortcoming of the model.

### C. Particle emission at equilibrium

Compared to PRECO-2000 simulations, the calculations performed with the code PREEQ have shown that this last approach allows a better description of the particle emission in the preequilibrium stage. For that reason, the results obtained with this model will be used in the further discussion.

As already discussed previously, the results presented in Figs. 22 and 23 suggest that for heavy targets, almost all particles are emitted during the preequilibrium phase of the reaction. Except for low-energy  $\alpha$  particles, the PREEQ calculated distributions allow a good description of the experimental results over the full energy range, showing that the contribution of the evaporation process should be small. On the other hand, for light target nuclei (Figs. 22 and 24), the

low-energy component of the experimental distributions suggest that the particle emission at equilibrium is rather important.

In this section, we propose to determine the contribution of the evaporation process. This component can be calculated separately assuming that it results from two different sources. The first source is the so-called “pure evaporation” and concerns the evaporation from the compound nucleus that has reached a statistical equilibrium. In Ref. [31], its contribution is given by a fraction  $f_{EQ}(E) = [1 - f_{PE}(E)]$  of the total reaction cross section, where  $f_{PE}(E)$  is the fraction of the preequilibrium emission, considering  $n$ ,  $p$ ,  $d$ ,  $t$ ,  $^3\text{He}$ , and  $\alpha$  particles, and  $E$  is the composite nucleus excitation energy. We determined this fraction using the preequilibrium spectra calculated with the PREEQ code for all ejectile types. The resulting value obtained for the 96 MeV  $^{56}\text{Fe}(n, X)$  reactions is  $f_{PE}(E) = 0.993$ , in agreement with that estimated for 62 MeV  $^{54}\text{Fe}(p, X)$  reactions in Ref. [32]. That value very close to 1 shows that almost the entire reaction cross section is available for the preequilibrium emission, and that the evaporation process of a compound nucleus represents a very small component with an associated value of  $f_{EQ}(E) = 0.007$ . The second source of the equilibrium component, which can be considered is the evaporation from a residual nucleus left in an excited state just after the preequilibrium emission has occurred. In order to estimate the excitation energy of such a nucleus and its formation probability after the preequilibrium emission of each outgoing particle type, again, we used the energy differential distributions previously calculated with PREEQ. The residual nucleus excitation energy is given by the formula  $U = E - B_\beta - e_\beta$ , where  $B_\beta$  and  $e_\beta$  are the binding energy of the emitted particle  $\beta$  and its emission energy, respectively, and  $E$  is the excitation energy of the compound nucleus. Having determined that quantity, the evaporation spectra are further calculated using the Hauser-Feshbach formalism [18]. Particles are emitted until the evaporation process is no longer energetically possible and the nucleus remaining energy is released in the form of  $\gamma$  rays.

The results obtained for the 96 MeV  $^{56}\text{Fe}(n, X)\text{lc}$  reactions are given in Fig. 28 (dotted lines), together with the preequilibrium component calculated with PREEQ as described in Sec. V A (dashed lines). The total particle emission spectrum determined by summing both mechanism contributions (continuous line) is also presented and compared to the experimental data (points). The agreement found over the full energy range is relatively good, except for helium isotopes around 20 MeV, where the calculated distributions are below the experimental results. The same effect has been found for the  $^{208}\text{Pb}(n, X^4\text{He})$  reaction, showing that the preequilibrium contribution for helium isotopes is underestimated in this energy region for both light and heavy targets. For hydrogen isotopes the introduction of the evaporation contribution allows a good description of the particle emission over a wide energy range.

### D. Angular distributions

To complete our analysis about the models, we would like to compare the experimental angular differential cross sec-

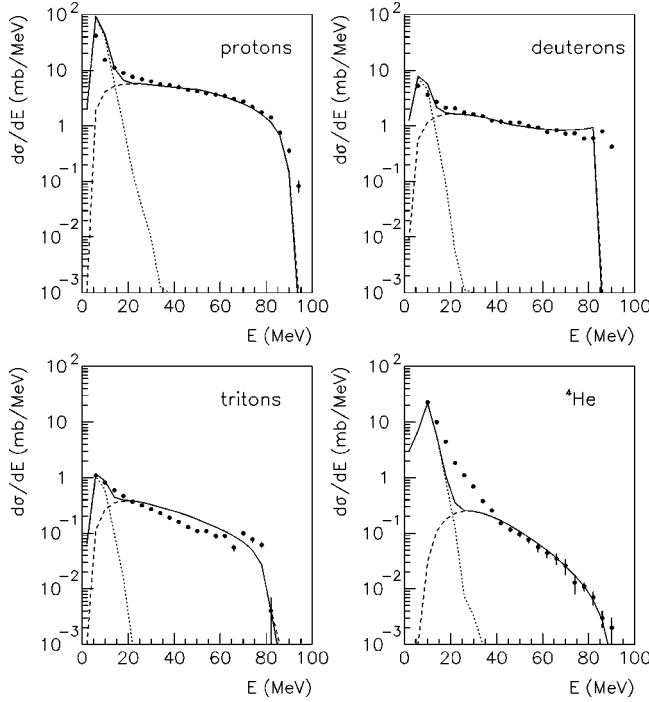


FIG. 28. Calculated preequilibrium and evaporation contributions (dashed and dotted lines, respectively) in the particle emission spectra for the 96 MeV  $^{56}\text{Fe}(n, X\text{lcp})$  reaction, compared to the experimental results of the present work (full circles). The calculated total distributions (sum of preequilibrium and evaporation spectrum) are presented as continuous lines.

tions to the theoretical ones. While the exciton model is largely used to calculate angle integrated energy spectra, the determination of angular distributions is out of its capabilities. In order to overcome this difficulty, several approaches involving modifications of the exciton model have been proposed, as in Ref. [33]. However, most of them contain serious approximations or induce computational complexities and they can be applied only for a limited set of reaction configurations. For this reason, a phenomenological approach proposed in Ref. [17] is often preferred to study the continuum angular distributions. It is based on a systematical study of a wide variety of experimental data. The parameterization established for the double-differential cross section as a function of the total energy-differential cross section is given by the equation:

$$\frac{d^2\sigma}{d\Omega de} = \frac{1}{4\pi} \frac{d\sigma}{de} \frac{a}{\sinh(a)} [\cosh(a \cos \theta) + f_{PE} \sinh(a \cos \theta)]. \quad (3)$$

In this expression,  $\theta$  is the emission angle in the center of mass frame, and the term  $a$  is the slope parameter depending on the incident particle type and energy, the target nucleus and the exit channel. It can be calculated using the procedure described in Ref. [17]. The  $f_{PE}$  parameter is the fraction of particle emission apart from equilibrium. It will be called further the fraction of preequilibrium emission and it is calculated using the formula

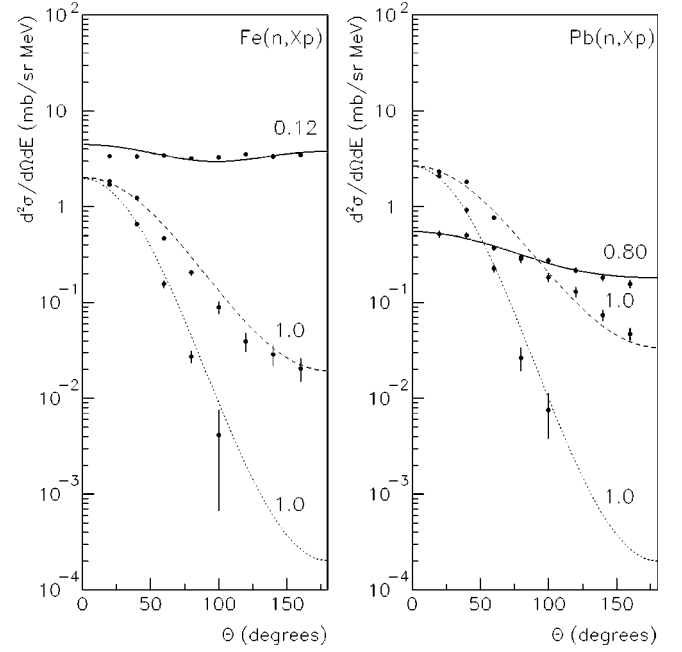


FIG. 29. Double-differential distributions calculated using the parameterization from Ref. [17] (lines) for proton emission in 96 MeV neutron-induced reactions on  $^{56}\text{Fe}$  and  $^{208}\text{Pb}$  compared with the experimental results (points). The continuous, dashed, and dotted lines correspond to the 8–12 MeV, 40–44 MeV, and 68–72 MeV emission energy ranges, respectively. The contribution of the preequilibrium emission in the total cross section ( $f_{PE}$  factor) for each domain is also given near the corresponding distribution.

$$f_{PE} = \frac{(d\sigma/de)_{PE}}{(d\sigma/de)} = \frac{(d\sigma/de)_{PE}}{(d\sigma/de)_{PE} + (d\sigma/de)_{EQ}}, \quad (4)$$

where the  $PE$  and  $EQ$  symbols refer respectively to preequilibrium and equilibrium emissions. Using the energy-differential cross sections for these two processes calculated in Secs. V A and V C, the double-differential cross sections are calculated according to Eq. (3). In Fig. 29 are presented the resulting angular distributions (lines) obtained for the proton emission in  $^{56}\text{Fe}(n, X)$  and  $^{208}\text{Pb}(n, X)$  reactions at 96 MeV (right and left figures, respectively), together with the experimental data (points). In order to have a better illustration of the different reaction mechanisms that contribute to the particle emission spectra (evaporation and preequilibrium emission), when we constructed the angular distributions, we chose three different energy domains: 8–12 MeV (continuous lines), 40–44 MeV (dashed lines), and 68–72 MeV (dotted lines). The contribution of the preequilibrium emission in the total cross section ( $f_{PE}$  factor) for each domain is also given near the corresponding distribution.

We observe in general satisfactory agreement between the theoretical results and the experimental distributions. At low energies (8–12 MeV), particles are emitted from both evaporation and preequilibrium processes whose respective contributions depend on the target nucleus mass. For the iron case, we found  $f_{PE}=0.12$  and we observe a quasi-isotropic distribution, both signals indicating that the evaporation pro-



cess is dominant for light targets. For the lead target,  $f_{PE}=0.80$  and the angular distribution is slightly forward peaked, showing that low-energy particles are mainly emitted during the preequilibrium stage. For more energetic particles,  $f_{PE}=1$  for both targets, and we observe that they are mainly emitted at small angles, following the beam direction. From this, we deduce that those ejectiles are emitted before an equilibrium has been reached. We found a similar agreement when we built the complex particle distributions, showing that the Kalbach parameterization is able to give a proper description of the double differential cross sections, whatever the target or the emitted particle. In addition, a physical basis for this parameterization has been established in Ref. [34], allowing a more detailed theoretical understanding of the properties of the angular distributions in the continuum energy domain.

## VI. SUMMARY

In this paper, we report a new set of experimental data concerning light-charged-particle production in 96 MeV neutron-induced reactions on natural iron, lead, and uranium targets. Double-differential cross sections of charged particles have been measured over a wide angular range ( $20^\circ - 160^\circ$ ). With the MEDLEY setup, data were measured for  $p$ ,  $d$ ,  $t$ ,  $^3\text{He}$  and  $\alpha$  particles, with low-energy thresholds. The SCANDAL setup has been used to measure proton production cross sections in the same angular range, with good statistics and angular resolution, but with an energy threshold of about 30 MeV. For proton emission, very good agreement found between both sets of measurements obtained with both independent detection systems shows that we had a good control of the systematical uncertainties involved. This is due, in part, to the unambiguous cross section normalization that has been applied using very accurate data on the  $np$  scattering cross section [13]. In our experiment, we also measured this cross section and we obtained a good agreement with data from Ref. [13]. The estimated systematical uncertainties affecting the double-differential cross sections reported in this work are of the order of 5%.

Data presented in this paper allow the extension to higher energies (up to 96 MeV) of the available experimental results on nucleon-induced reactions in the 20–200 MeV energy range, which were up to now limited to about 60 MeV incident energy. This new data set, together with the data already existing in the literature, allows us to study in detail both main theoretical approaches [3,4] available nowadays for the description of nucleon and complex particle emission in nucleon-induced reactions at intermediate energies. These approaches have been proposed mainly to improve the exciton model predictions concerning the production of clusters, which was originally strongly underestimated by the model, as shown with the calculations we have performed with the GNASH code [6]. Since the cross sections evaluated with GNASH are at present implemented in the MCNPX code, we would like to issue a warning that some important information needed in specific application as the power deposited in a spallation target of an ADS could be underestimated.

In order to test both approaches, we performed calculations

with the PREEQ [20] and PRECO-2000 [28] codes. The PREEQ results have shown that by taking into account the cluster formation probability in the preequilibrium stage of the reaction, one can obtain a global agreement over a wide set of configurations. The formation probability is a free parameter in the PREEQ code and we have adjusted it for each target nucleus. The evolution of the resulting values shows that, for a given outgoing particle, the probability decreases with the target mass. In addition, for a given target, the formation probability is larger for lighter particles. This parameter depends very little on the incident particle type and energy. Proposed as an alternative to this approach, the method used in the PRECO-2000 code and implemented in the more recent code TALYS [29] to calculate complex particle production cross sections considers contributions of direct reactions in the outgoing spectra. In many cases, however, this approach does not lead to a good reproduction of the experimental distributions. Despite the acceptable agreement found in some particular situations, it cannot be used for the moment in a global description of nucleon-induced reactions. This deficiency is due in part to the strong dependence of its predictions on the projectile type. It is our hope that the work performed at present in the development of the TALYS code will soon provide an improved version of this approach.

We have completed the description of the particle emission over the full energy range by adding the contribution of the evaporation process to the preequilibrium emission calculated using the PREEQ code. That calculation scheme has shown that for heavy targets, almost all particles are emitted during the preequilibrium stage of the reaction, while for light targets, a strong component from the evaporation process is present at low emission energy. In addition, the most important contribution in the equilibrium component originates from the decay of residual nuclei left in an excited state after the preequilibrium particle emission. Finally, we have shown that a correct description of the energy-differential distributions and of the different mechanisms contributing to the total cross section allows us to calculate double-differential cross sections by including also the parameterization from Ref. [17] for the angular distribution determination. The good reproduction of the shapes of the double-differential distributions that we obtained with this method suggests that theoretical models must provide at least a good description of the energy-differential cross sections. The parameterization established in Ref. [17] allows a more detailed study of the reaction with a rather satisfactory accuracy by allowing the prediction of the double-differential distributions.

The results presented in this work show that the understanding of nucleon-induced reactions at these energies is far from complete. Two approaches are available in the framework of the exciton model for the description of cluster emission in these specific reactions and among them, only that based on the coalescence model seems to have a satisfactory predictive power. It is, however, based on a scale factor associated with the formation probability of complex particles, which has to be adjusted to experimental data. Therefore, further theoretical progress must be done in this field in order to improve the existing theoretical approaches of the exciton model and to provide new models based on

different considerations. An alternative has been recently proposed in this direction, which uses the wavelet technique to simulate the nuclear dynamics and whose results are very encouraging. They will constitute the subject of a future publication [35].

### ACKNOWLEDGMENTS

This work was supported by the European Community under the HINDAS project (Contract No. FIKW-CT-2000-

0031), the GDR GEDEON (Research Group CEA-CNRS-EDF-FRAMATOME), Vattenfall AB, the Swedish Nuclear Fuel and Waste Management Company, the Swedish Nuclear Power Inspectorate, Barsebäck Power AB, Ringhals AB, the Swedish Defence Research Agency, and the Swedish Research Council. We would like to thank the TSL staff for assistance and quality of the neutron beam. We are also grateful to Dr. E. Betak for very useful discussions concerning calculations with the PREEQ code. Special thanks to Dr. C. Kalbach for her significant contributions to the progress of theory in nucleon-induced reactions.

- 
- [1] HINDAS: High and Intermediate Energy Nuclear Data for Accelerator-Driven Systems, European Community, Contract No. FIKW-CT-2000-0031.
  - [2] J. J. Griffin, *Phys. Lett.* **17**, 478 (1966).
  - [3] I. Ribanský and P. Obložinský, *Phys. Lett.* **45B**, 318 (1973).
  - [4] C. Kalbach, *Z. Phys. A* **283**, 401 (1977).
  - [5] J. R. Wu and C. C. Chang, *Phys. Rev. C* **17**, 1540 (1978).
  - [6] P. G. Young, E. D. Arthur, and M. B. Chadwick, "Comprehensive Nuclear Model Calculations: Introduction to the Theory and Use of the GNASH Code," Report No. LA-12343-MS, 1992.
  - [7] A. N. Smirnov, V. P. Eismont, and A. V. Prokofiev, *Radiat. Meas.* **25**, 151 (1995).
  - [8] S. Dangtip, A. Ataç, B. Bergenwall, J. Blomgren, K. Elmgren, C. Johansson, J. Klug, N. Olsson, G. Alm Carlsson, J. Söderberg, O. Jonsson, L. Nilsson, P.-U. Renberg, P. Nadel-Turonski, C. Le Brun, F.-R. Lecolley, J.-F. Lecolley, C. Varignon, Ph. Eudes, F. Haddad, M. Kerveno, T. Kirchner, and C. Lebrun, *Nucl. Instrum. Methods Phys. Res. A* **452**, 484 (2000).
  - [9] J. Klug, J. Blomgren, A. Ataç, B. Bergenwall, S. Dangtip, K. Elmgren, C. Johansson, N. Olsson, S. Pomp, A. V. Prokofiev, J. Rahm, U. Tippawan, O. Jonsson, L. Nilsson, P.-U. Renberg, P. Nadel-Turonski, A. Ringbom, A. Oberstedt, F. Tovesson, V. Blideanu, C. Le Brun, F.-R. Lecolley, J.-F. Lecolley, M. Louvel, N. Marie, C. Schweitzer, C. Varignon, Ph. Eudes, F. Haddad, M. Kerveno, T. Kirchner, C. Lebrun, L. Stuttgé, I. Slypen, A. N. Smirnov, R. Michel, S. Neumann, and U. Herpers, *Nucl. Instrum. Methods Phys. Res. A* **489**, 282 (2002).
  - [10] H. Condé, S. Hultqvist, N. Olsson, T. Rönqvist, R. Zorro, J. Blomgren, G. Tibell, A. Häkansson, O. Jonsson, A. Lindholm, L. Nilsson, P.-U. Renberg, A. Brockstedt, P. Ekström, M. Österlund, F. P. Brady, and Z. Szefflinski, *Nucl. Instrum. Methods Phys. Res. A* **292**, 121 (1990).
  - [11] J. F. Ziegler, *The Stopping and Range of Ions in Solids* (Pergamon, Elmsford, NY, 1985).
  - [12] GEANT Detector Description and Simulation Tool, CERN Program Library Long Write-up W5013.
  - [13] J. Rahm, J. Blomgren, H. Condé, S. Dangtip, K. Elmgren, N. Olsson, T. Rönqvist, R. Zorro, O. Jonsson, L. Nilsson, P.-U. Renberg, A. Ringbom, G. Tibell, S. Y. van der Werf, T. E. O. Ericson, and B. Loiseau, *Phys. Rev. C* **63**, 044001 (2001).
  - [14] P. W. Lisowski, R. E. Shamu, G. F. Auchampaugh, N. S. P. King, M. S. Moore, G. L. Morgan, and T. S. Singleton, *Phys. Rev. Lett.* **49**, 255 (1982).
  - [15] T. Rönqvist, H. Condé, E. Ramström, R. Zorro, J. Blomgren, A. Häkansson, A. Ringbom, G. Tibell, O. Jonsson, L. Nilsson, P.-U. Renberg, S. Y. van der Werf, W. Unkelbach, and F. P. Brady, *Nucl. Phys.* **A563**, 225 (1993).
  - [16] A. Guertin, N. Marie, S. Auduc, V. Blideanu, Th. Delbar, Ph. Eudes, Y. Foucher, F. Haddad, T. Kirchner, Ch. Le Brun, C. Lebrun, F.-R. Lecolley, J.-F. Lecolley, X. Ledoux, F. Lefebvres, M. Louvel, A. Ninane, Y. Patin, Ph. Pras, G. Rivière, and C. Varignon (to be published).
  - [17] C. Kalbach, *Phys. Rev. C* **37**, 2350 (1988).
  - [18] W. Hauser and H. Feshbach, *Phys. Rev.* **87**, 366 (1952).
  - [19] H. Machner, *Phys. Lett.* **86B**, 129 (1979).
  - [20] K. K. Gudima, S. G. Mashnik, and V. D. Toneev, *Nucl. Phys.* **A401**, 329 (1983).
  - [21] GEANT4 Physics Reference Manual, <http://wwwasd.web.cern.ch/wwwasd/geant4/geant4.html>.
  - [22] E. Betak, *Comput. Phys. Commun.* **9**, 92 (1975).
  - [23] M. Blann, R. R. Doering, A. Galonski, D. M. Patterson, and F. E. Serr, *Nucl. Phys.* **A257**, 15 (1976).
  - [24] F. E. Bertrand and R. W. Peele, *Phys. Rev. C* **8**, 1045 (1973).
  - [25] H. Machner, *Phys. Rev. C* **21**, 2695 (1980).
  - [26] T. C. Awes, G. Poggi, C. K. Gelbke, B. B. Back, B. G. Glagola, H. Breuer, and V. E. Viola, Jr., *Phys. Rev. C* **24**, 89 (1981).
  - [27] H. H. Gutbrod, A. Sandoval, P. J. Johansen, A. M. Poskanzer, J. Gosset, W. G. Meyer, G. D. Westfall, and R. Stock, *Phys. Rev. Lett.* **37**, 667 (1976).
  - [28] C. Kalbach-Walker, users manual for PRECO-2000, 2001.
  - [29] A. Koning (unpublished).
  - [30] M. Kerveno, F. Haddad, Ph. Eudes, T. Kirchner, C. Lebrun, I. Slypen, J. P. Meulders, C. Le Brun, F. R. Lecolley, J. F. Lecolley, M. Louvel, F. Lefebvres, S. Hilaire, and A. J. Koning, *Phys. Rev. C* **66**, 014601 (2002).
  - [31] J. R. Wu and C. C. Chang, *Phys. Rev. C* **16**, 1812 (1977).
  - [32] J. R. Wu and C. C. Chang, *Phys. Lett.* **60B**, 423 (1976).
  - [33] G. Mantzouranis, D. Agassi, and H. A. Weidenmüller, *Phys. Lett.* **57B**, 220 (1975).
  - [34] M. B. Chadwick and P. Obložinský, *Phys. Rev. C* **50**, 2490 (1994).
  - [35] F. Sébille, C. Bonilla, V. Blideanu, and J.-F. Lecolley (to be published).